Biol635/Math635/Biol432/Math430
Fall 2022
.
Assignment 4

Answer the following questions.

- Justify your answers.
- Explain your results.
- Provide the necessary calculations in a clear way.
- Provide the necessary supporting graphs and codes.
- Make sure the graphs are properly labeled and include the information (title and parameter values) necessary to understand your explanations.

Question 1

Build an isopotential model of Hodgkin-Huxley type using the following parameters: $C = 1\,\mu F/cm^2$, $E_L = -52\,mV$, $E_{Na} = 55\,mV$, $E_K = -75\,mV$, $G_L = 0.3\,mS/cm^2$ $G_{na} = 120\,mS/cm^2$ and $G_K = 36\,mS/cm^2$. Leave I_{app} as a free parameter. The activation (m) and inactivation (h) gating variables for the Na-current have powers of 3 and 1 respectively. The activation gating variable (n) for the K-current has a power of 4. The voltage-dependent activation/inactivation curves and time-scales are given by

$$m_\infty(V) = \frac{1}{1 + e^{-(V+40)/9}},$$

$$h_\infty(V) = \frac{1}{1 + e^{(V+62)/10}},$$

$$n_\infty(V) = \frac{1}{1 + e^{-(V+53)/16}},$$

$$\tau_m(V) = 0.3,$$

$$\tau_h(V) = 1 + \frac{11}{1 + e^{(V+62)/10}},$$

and

$$\tau_n(V) = 1 + \frac{6}{1 + e^{(V+53)/16}}.$$

Apply a square pulse of applied current (I_{app}) of 2 sec duration and amplitude I_0 (μA). (Make sure that you allow a few msec pass before you apply the current pulse; depending on the initial conditions of the activation and inactivation variables you will get transients that you must disregard. A conservative value would be 1 sec.)

(a) Plot the activation/inactivation functions $m_\infty(V)$, $h_\infty(V)$ and $n_\infty(V)$ (one graph).

(b) Plot the voltage-dependent time constants $\tau_m(V)$, $\tau_h(V)$ and $\tau_n(V)$ (one graph)

(c) Plot the voltage traces (graphs of V vs. t) for $I_{app} = 0, 1, 2, 3, 4$.

(d) Plot a freq. vs. I_{app} graph for this current pulse duration and $I_{app} \in [0 : 4]$. The graph must contain at least 10 points.

Question 2

Build a code to model the inhibitory cell in the following paper: "Kopell, Ermentrout, Whittington, Traub; Gamma rhythms and beta rhythms have different synchronization properties; PNAS (1999)"

(a) Plot the activation/inactivation functions $m_\infty(V)$, $h_\infty(V)$ and $n_\infty(V)$ (one graph).

(b) Plot the voltage-dependent time constants $\tau_m(V)$, $\tau_h(V)$ and $\tau_n(V)$ (one graph)

(c) Simulate the model during 10 sec for values of I_{app} within the range $[0.1190, 0.12]$ (11 points at least) and then within the range $[0.12, 0.15]$ (11 points at least).

(d) Plot a freq. vs. I_{app} graph.

Question 3 (graduate)

What is the main difference between the voltage patterns of the two models? How can you explain them?

Gamma rhythms and beta rhythms have different synchronization properties

N. Kopell[†‡], G. B. Ermentrout[§], M. A. Whittington[¶], and R. D. Traub[‖]

[†]Department of Mathematics and Center for BioDynamics, Boston University, Boston MA 02215; [§]Department of Mathematics, University of Pittsburgh, Pittsburgh PA 15260; [¶]School of Biomedical Sciences, Worsley Building, University of Leeds, Leeds LS2 9NL, United Kingdom; and [‖]Division of Neuroscience, The Medical School, University of Birmingham, Birmingham B15 2TT, United Kingdom

Contributed by Nancy J. Kopell, December 3, 1999

Experimental and modeling efforts suggest that rhythms in the CA1 region of the hippocampus that are in the beta range (12–29 Hz) have a different dynamical structure than that of gamma (30–70 Hz). We use a simplified model to show that the different rhythms employ different dynamical mechanisms to synchronize, based on different ionic currents. The beta frequency is able to synchronize over long conduction delays (corresponding to signals traveling a significant distance in the brain) that apparently cannot be tolerated by gamma rhythms. The synchronization properties are consistent with data suggesting that gamma rhythms are used for relatively local computations whereas beta rhythms are used for higher level interactions involving more distant structures.

Rhythms in the gamma range (30–80 Hz) and the beta range (12–30 Hz) are found in many parts of the nervous system and are associated with attention, perception, and cognition (1–3). It has been noted in electroencephalogram (EEG) signals that rhythms of different frequencies are found simultaneously (4). Beta oscillations are readily observable immediately after evoked gamma oscillations in sensory evoked potential recordings (5). This beta activity has been correlated with the long-range synchronous activity of neocortical regions during visuomotor reflex activation (6).

This paper concerns the correlation between the frequency band of coherent oscillations and conduction delays between the sites participating in the coherent rhythm. It has been noted (7) in human EEG subjects that gamma rhythms are prevalent in local visual response synchronization, but more distant coherence occurring during multimodal integration between parietal and temporal cortices uses rhythms at frequencies of 12–20Hz (the so-called beta 1 range).

We shall use data from the CA1 region of the hippocampus (8–10) as a paradigm to address the questions of how long-distance synchrony is achieved and why there is a correlation between oscillation frequency and the temporal distances between participating sites. The data available from the rat hippocampus slice preparation give clues about details of dynamics that are important to the synchronization process.

The work builds on earlier work (11–12) describing and analyzing the role of doublet spikes in interneurons in producing synchrony when there are significant conduction delays. Earlier work (13) using rate models showed, via simulations, that longer conduction delays could be tolerated and still produce synchrony if the carrier rhythm had lower frequencies. However, a rate model is not consistent with the situation in which excitatory cells fire at most one spike per cycle, and with high precision in phase. An alternative solution was suggested by data and large-scale models of the gamma rhythm in the hippocampus (8, 9). In both data and models, the ability to synchronize happened in those parameter regimes in which interneurons produced a spike doublet in many of the cycles. This mechanism was analyzed by Ermentrout and Kopell (11), where it was shown how the doublet provides a feedback mechanism for the timing. The analysis given there predicted that, for long conduction delays (above 8–10 ms, depending on network parameters), synchronization in the gamma frequency band is not robust. Although conduction delays in the neocortex are variable, there is evidence that the delays between association areas could be significantly larger than 10 ms (see *Discussion*).

In this paper, we show that the beta rhythm observed in the hippocampal slices is not merely a slower version of gamma, but has a distinct dynamical structure and makes use of intrinsic membrane currents not expressed during gamma. Furthermore, the beta rhythm is much better adapted to synchronization in the presence of long conduction delays. Via a very reduced model, we analyze why this is so. Predictions from the analysis are shown to hold in the large-scale models.

Background on production of beta and gamma rhythms in the hippocampal slice can be found in ref. 3. In the tetanic stimulation paradigm (9, 10), with sufficiently strong stimuli, the hippocampal slice produces both gamma and beta, with a transition between them. In intracellular recordings of beta in pyramidal cells, gamma-frequency oscillations continue between beta-frequency population spikes, suggesting that the interneuron network continues to oscillate at gamma frequency, which the pyramidal cells cannot follow (Fig. 1*A*). Two system parameters alter in time before and during the transition to beta: the strength of recurrent excitatory synapses and the amplitude of one or more slow K conductances. Both of these parameters increase and then level off, and experimental data and large-scale simulations suggest that evolution of both parameters is necessary for the switch to beta to occur (10, 14). Beta oscillations are synchronized between the two sites when both sites are stimulated together intensely (10, 14).

In human EEG, occurring spontaneously or evoked by auditory stimulation by novel sounds, power in the gamma range coexists with beta, consistent with the beat-skipping structure [C. Haenschel and J. Gruzelier, personal communication; also see the work by Tallon-Baudry *et al.* (15)].

Local Inhibition-Based Rhythms. The data and large scale simulations cited above all concern the behavior of the network when two sites are intensely stimulated together. To better understand the mechanism behind the network behavior, we first consider the behavior at one site. We show, via very reduced models, that the transition from gamma to beta can be understood as a consequence of the changes in recurrent excitatory synapses and expressions of K-conductances. Although this had previously been documented in large-scale simulations (14), the ability of the small network to reproduce this creates an excellent model within which to understand more deeply the long-distance synchronization properties of beta and gamma.

We use models that are much reduced from the large scale simulations in two ways. The network is pared down to a minimal number of cells and connections. We work with a local network of two pyramidal cells (excitatory, or E-cells) and two interneurons (inhibitory, or I-cells). All cells are coupled to one another, except

---

Abbreviation: EEG, electroencephalogram; AHP, after-hyperpolarization.

[‡]To whom reprint requests should be addressed. E-mail: nk@bu.edu.

The publication costs of this article were defrayed in part by page charge payment. This article must therefore be hereby marked "*advertisement*" in accordance with 18 U.S.C. §1734 solely to indicate this fact.

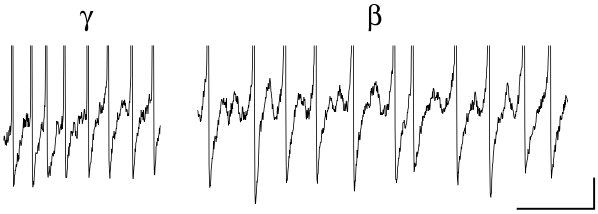

Fig. 1. Gamma and beta oscillations *in vitro*. Intracellular recordings of gamma and beta oscillations in a CA1 hippocampal pyramidal neuron. Oscillations were induced by brief tetanic stimulation [see Whittington *et al.* (9) for methods]. The initial posttetanic response is a gamma oscillation with action potentials (frequency 38 Hz) separated by a period of hyperpolarization made up of both AHP and inhibitory synaptic activity. After the transition to beta activity, the underlying gamma membrane potential oscillation is still apparent (frequency 42 Hz), but spiking occurs on every second or third period (frequency 18 Hz). Action potentials are separated by the initial AHP/IPSP hyperpolarization and additional IPSPs. (Bar = 1 mV, 100 ms.)

possibly for coupling between the excitatory cell (dotted lines in Fig. 2*A*). E-E coupling, although sparse in the CA1 (16), turns out to be important for the beta rhythm (10, 14); gamma rhythms, however, can be simulated without E-E coupling (11, 17). The gamma rhythm corresponds to one in which all of the cells fire synchronously at 30–70 Hz whereas in the beta rhythm, the I-cells synchronize at a gamma frequency and the E-cells synchronize at a frequency half as fast. Compared with the detailed biophysical models (14), the cells are also simple: they are modeled as single compartment cells with fast spiking currents for the gamma rhythm; for the beta rhythm, an extra after-hyperpolarization (AHP) current (slow K conductance) is added to the E-cells (see *Appendix*). Although we use a specific current (M-current) in the simulations, the analysis in the mathematics given below will work for any AHP current with the appropriate decay time.

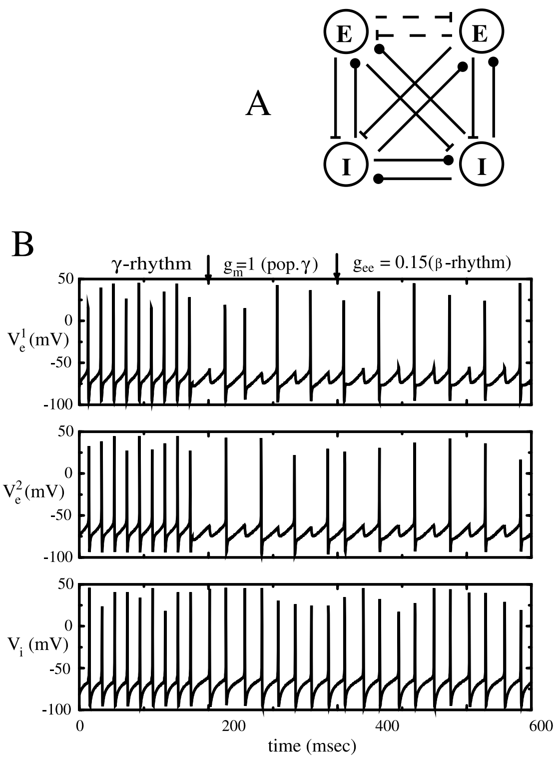

Fig. 2. (*A*) Minimal network for investigating local synchronization of gamma and beta rhythms. For the gamma rhythms, the E-E connections are absent; for the beta rhythms, they are a necessary part of the circuit. (*B*) Gamma-to-beta transition of local rhythms occurs as the AHP is turned on and the local E-E connections are strengthened. Parameters are as in the appendix. For the gamma rhythm, $g_{ee} = 0$ and $g_m = 0$. At the first arrow, g_m is set to 1, switching the rhythm from gamma to a rhythm in which the E-cells miss beats and fires nonsynchronously. At $t = 400$, $g_{ee} = 0.15$, and the network quickly suppresses the nonsynchronous solution, leaving only the synchronous local state. Throughout the transitions, the I cells shown below exhibit only minor changes, slowing down slightly because of the decreased excitation (excitation every other cycle).

Increases in K-conductances, plus increases in the strength of synapses between excitatory cells, can transform the output of the network of E and I cells from gamma to beta. This transformation was documented in the detailed biophysical model (14) with two connected sites. In Fig. 2*B*, we show that the transition is reproduced in the reduced model, even without the synaptic connections between the sites. The first part of Fig. 2*B* displays the voltage traces of the two E-cells and one of the I-cells (they are synchronous) with parameters that elicit a gamma rhythm. In the middle section, a slower K-conductance has been added to the model E-cells; now the E-cells, slowed down by the K-conductance, each fire on half of the gamma cycles. Note that they fire on opposite cycles. For the third part of Fig. 2*B*, the parameters were further changed by adding synaptic (AMPA-mediated) connections between the E-cells; the network is now as in Fig. 2*A* with the dotted lines. Now the E-cells still fire every other cycle, but this time on the same cycle; that is, they produce beta.

To understand why the E-cells miss opposite cycles in the absence of the E-E coupling, we note that the firing of one E-cell effectively silences the other in a given cycle through feedback inhibition, unless the lagging cell is so close that it fires before the onset of the feedback inhibition. A major effect of the mutual excitatory connections is to increase the range of initial conditions under which the second cell can fire before receiving inhibition; in a manner graded with the size of the excitatory conductance, the excitation advances the firing of the second E-cell, preventing suppression in that cycle.

With some E-E coupling, there can be other initial conditions for the same parameters for which the E-cells do fire on opposite cycles throughout the trajectory. However, if the E-E coupling is sufficiently large, that solution does not stably exist. With enough excitation from the cell that fires in a given cycle, the other cell is forced to fire in the same cycle, ruling out the solution in which cells fire on opposite cycles.

We also note that there are many different ways to change parameters to produce the gamma-to-beta transition. In addition to the new excitatory connections, the essential change is to lower the excitability of the E-cells relative to the I-cells, by changing relative drives or intrinsic conductances. As we will see in the next section, synaptic input from distant sources can also change the balance of excitability.

Long-Distance Synchronization in Inhibition-Based Rhythms. *Strategy and basic dynamical properties.* The different dynamical structures and currents associated with gamma and beta lead to different results when these rhythms are used to coordinate dynamical activity of loci at a distance from one another. To show this, our strategy is to look at the dynamics near the gamma or beta rhythm and create a map (a function relating the timing of one cycle to that of the next) containing information about whether, and in what parameter ranges, that rhythm is dynamically stable.

There are two principles that govern the behavior of the maps. The first is that E-cells are able to fire when inhibition, either synaptic or intrinsic (from AHP currents), has worn off sufficiently. This situation obtains when the effective membrane time constant of the excitatory cells is small compared with the decay time of the synaptic current and/or the AHP current; the voltage then tracks the time course of the synapses or AHP currents.

Second, the I-cells have an extra property, associated with relative refractory period. Suppose a cell fires at $t = 0$ and receives

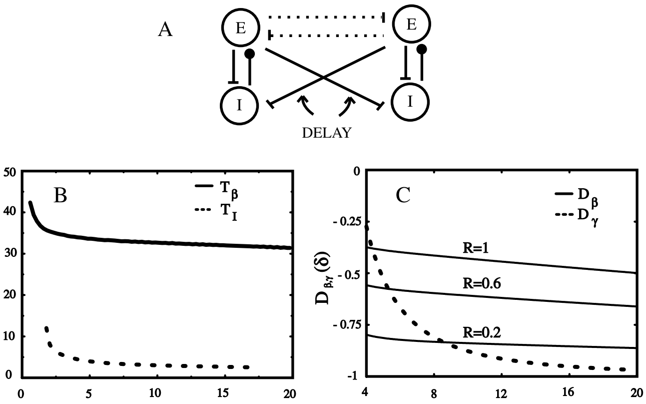

Fig. 3. (*A*) Minimal network for investigating synchronization with conduction delays. The long E-E connections are essential for coherence of the beta rhythm across distances, but not for the gamma rhythm. (*B*) The maps T_I and T_β as a function of the delay δ for $g_m = 1$ and all others parameters as in the Appendix. All axes have units of milliseconds. (*C*) The linearized scaling factor *D* for the gamma rhythm (dashed) and for the beta rhythm at various ratios of the effective AHP conductance and the effective inhibitory synaptic conductance. The closer *D* is to zero, the faster the convergence to the synchronized state and the stronger is robustness to heterogeneity.

sufficiently large excitation again at $t = \psi > 0$. The cell fires again at $t = T_I(\psi)$, where T_I decays with ψ. That is, the more recovered the cell, the shorter the time to fire after a given fixed excitation. For ψ very short, the cell may not fire at all. T_I is related to the intrinsic refractory period of the I-cells but is influenced by the rest of the network. For example, increasing the self-inhibition in the local network increases the values of T_I. Standard integrate and fire neurons do not have this property, but it can be shown from simulations that this property does hold for biophysical models of the interneurons (11, 18). It also holds for more elaborate versions of integrate and fire equations (12).

An architecturally minimal model combines all local cells of a given type if they are synchronous in that rhythm. Thus, in both gamma and beta, a minimal model of the local circuit uses only one E cell and one I cell. In each of these, the model for long-distance interaction consists of two local circuits, with connections from E cells to the distant I cells (Fig. 3A, without the dotted lines). We also explore the effects of adding long connections between the E cells (Fig. 3*A*, dotted lines).

Gamma rhythms, beta rhythm, and feedback loops for two-site synchronization. In previous papers (8, 11, 12), we introduced a mechanism for long distance synchronization in gamma. In its simplest form, a network embodying this mechanism has two minimal local circuits, as in Fig. 3*A* without the dotted lines. The synchronization depends on operating in a parameter range in which the I-cells produce double spikes per cycle ("doublets"). The first spike of the doublet is temporally tied to excitation from the local E-cell; the second is caused by excitation from the distant E-cell. The timing between the doublets in a given cycle includes not only the difference in firing time between the two E-cells and the conduction delay, but a nonlinear property of the I-cells associated with relative refractory period. It is this nonlinearity that provides the feedback responsible for the synchronizing properties of the doublet configuration in the gamma rhythm. For the beta rhythm, there is an additional nonlinearity attributable to the AHP current. We show below how the extra current and the beat-skipping structure change the maps, and why this leads to tolerance of longer conduction delays for the beta rhythm.

Let t_1 and t_2 be the times of firing of cells E_1 and E_2 on some cycle, with $\Delta = t_1 - t_2$. Starting with the gamma rhythm, if the initial conditions are close enough to synchrony ($\Delta = 0$), we can construct a map that gives the times $\bar{t}_1$ and $\bar{t}_2$ of firing in the next cycle. The time at which the inhibition for an E-cell wears off enough for it to fire is approximated by the time at which the inhibitory conductance had decayed enough. [That this is an excellent approximation is easily checked by comparing simulations from the biophysical models with predictions using that approximation (11).] The latter threshold depends on the drive to the E-cells. We assume that there is saturation of the synapse from the I to the E cell, so that it is only the timing of the second spike of the doublet that determines when the postsynaptic E-cell will fire.

Cell I_1 is essentially recovered from firing in the previous cycle when it receives excitation from E_1 at t_1. (We assume no local conduction delay.) Hence, it fires a short (history independent) time, t_{ei}, later. (This time can be arbitrarily small, depending on the drive to the I-cells, but the latter drive may not be so large that the I-cells fire before the E-cells.) Cell I_1 receives excitation from E_2 at time $t_2 + \delta$, where δ is the delay time between the circuits. Cell I_1 then fires the second spike of its doublet at $t_2 + \delta + T_I(t_2 + \delta - t_1 - t_{ei}) = \hat{T}_I$. E_1 fires in the next cycle when the inhibitory conductance equals some threshold level g_*, i.e., at a time $\bar{t}_1$ defined by

$$g_{ie}\exp[-(\bar{t}_1 - \hat{T}_I)/\tau] = g_*, \qquad [1]$$

where τ is the time constant for decay of inhibition. g_* is related to the drive to the cell via the intrinsic period p_γ induced by that drive in an uncoupled cell, namely $g_{ie}\exp[(-p_\gamma + t_{ei})/\tau] = g_*$. From the above, we can compute the time $\bar{t}_1$ in terms of t_1 and t_2 and similarly for $\bar{t}_2$.

The map for analysis of the dynamics near the beta rhythm is a variation of Eq. **1**, with two modifications. The cell I_1 now fires three spikes per beta cycle, two during the gamma cycle in which the E-cells fire, and one during the cycle in which the E-cells are silent. The excitation from the distant cell is, as before, received by an I-cell after it has fired its first spike of the period. The map T_I for the gamma rhythm is replaced by T_β, which is defined to be the interval between the time cell I_1 receives excitation from cell 2 and the time it fires its third (not second, as before) spike; T_β depends on the times t_1, t_2, defined as above. Thus, the time at which the third spike of the I cell fires is $t_2 + \delta + T_\beta(t_2 + \delta - t_1 - t_{ei}) \equiv \hat{T}_\beta$. Fig. 3*B* shows T_I, T_β. Note that, in this parameter range, T_β is almost T_I plus a constant. As shown in ref. 11, it is the slope of the map T_I (or T_β) that matters in determining whether synchronization will take place; thus, this is not the key alteration that changes the synchronization properties.

The second modification introduces an intrinsically based source of inhibition, namely the slowly decaying AHP current of the E-cells, with time constant τ_{ahp}, triggered by a spike of that cell. The time $\bar{t}_1$ of the next E_1 spike, determined by the time of the last inhibitory pulse received from cell I_1 and the previous E_1 spike time, is then defined implicitly by

$$g_{ie}\exp[-(\bar{t}_1 - \hat{T}_\beta)/\tau] + g_{ahp}\exp[-(\bar{t}_1 - t_1)/\tau_{ahp}] = g_{*\beta}. \qquad [2]$$

Here g_{ahp} is an "effective conductance" that takes into account the actual maximal conductance $\bar{g}_{ahp}$ but scales it using the maximal value of the gating variable for that current and the ratio of the driving force of the AHP current to that of the synaptic current. To derive the threshold value $g_{*\beta}$, suppose an uncoupled local circuit displays a beat-skipping beta rhythm, and let t_{II} be the difference in time between the first and second I-spikes in a cycle. (Recall that, for the uncoupled beta rhythm, there are only two spikes per cycle.) Then, $g_{*\beta} = g_{ie}\exp[-(p_\beta - t_{II})/\tau] + g_{ahp}\exp[-p_\beta/\tau_{ahp}]$, where p_β is the period of the uncoupled beta rhythm.

To understand the implication of these maps for stability, we do a stability analysis with the implicit formula Eq. **3** by linearizing around the synchronous solution; we will show that the map of Eq. **1** can be considered a special case when there is no AHP. To do this, we define $\rho_i \equiv \bar{t}_i - t_i - p_\beta$, the variation in a given cycle from the periodic rhythm with period p_β. Δ is defined as before. We can rewrite Eq. **2** as

$$g_* = g_{ie}\exp[-(p_\beta + \rho_1 - \Delta - \delta - T_\beta(\Delta + \delta - t_{ei}))/\tau] + g_{ahp}\exp[-(p_\beta + \rho_1)/\tau_{ahp}]. \tag{3}$$

To lowest order in the small quantities Δ, ρ_1, ρ_2, the above can be expressed as

$$A\rho_1 + B(\rho_1 - \Delta(1 + T'_\beta(\delta - t_{ei})/\tau)) = 0,$$

where $A = (g_{ahp}/\tau_{ahp})\exp(-p_\beta/\tau_{ahp})$ and $B = (g_{ie}/\tau)\exp(-(p_\beta - \delta - T_\beta(\delta - t_{ei}))/\tau)$. (See *Appendix* for more details about A and B.) A similar formula holds for ρ_2, with Δ replaced by $-\Delta$. Subtracting these two formulae, and noting that $\rho_2 - \rho_1 = \bar{\Delta} - \Delta$, we have

$$(A + B)(\bar{\Delta} - \Delta) = -2B\Delta(1 + T'_\beta(\delta - t_{ei})/\tau))$$

$$\bar{\Delta} = \frac{A - B - 2BT'_\beta(\delta - t_{ei})/\tau}{A + B}\Delta \equiv D\Delta \tag{4}$$

Synchrony is stable if the coefficient D of Δ in Eq. **4** lies between -1 and $+1$. The closer Eq. **4** is to the stability boundary, the slower the synchronization, so the fastest synchronization occurs when $D = 0$; similarly, when the system is close to its stability boundary, small differences in local circuits can produce significant phase lags between the circuits. Fig. 3*C* shows D as a function of δ for other parameters as used in the simulations.

Eq. **4** and Fig. 3*B* reveal that there are two effects associated with synchronization. For short conduction delays, T'_β is significant and affects synchronization. For larger conduction delays (e.g., $\delta > 10$ ms), T'_β is essentially zero, and the synchronization comes from a balance between the decay of the inhibition (encoded in B, and dependent on δ) and the decay of the AHP current. Fig. 3*C* shows that increasing the amount of the AHP current brings D significantly closer to zero, increasing the robustness and rate of synchronization. See *Appendix* for information about the calculation of D and estimation of the quantities in Eq. **4**. The analysis for the gamma rhythm gives rise to a similar relationship as Eq. **4**, in which the expression T_β is replaced by T_I and the coefficient A is set to zero because there is no AHP current. In this case, there is no balance between the decay of inhibition and the AHP current, so all synchronization effects come from the non-zero slope of T_I; the latter function is essentially flat by 8–10 ms, which gives the critical constraint on long-distance synchronization in the gamma rhythm. As shown in ref. 11, changes in parameters do not significantly affect this conclusion.

Fig. 4 shows that the conclusions of the analysis hold for large scale networks as well as small ones. Fig. 4*A* shows a large-scale realistic model (14), showing the gamma-to-beta transition for E and I cells. The lower panels shows that there is synchronization in both frequency regimes. The right-hand panels of Fig. 4*A* show the same quantities when an extra 10-ms decay has been added to the conduction times between the two sites (in Fig. 4*A*, the cells are distributed, with a smaller maximal conduction delay across the total array of ≈4 ms). Note that the beta rhythm synchronizes across the two sites whereas the gamma rhythms in the two sites are in antiphase.

Effects of mutual excitation. The analysis we did above for synchronization between two distant sites used as signals only excitation to distant I-cells. Because there can also be mutually excitatory connections (as in Fig. 3*A* with the dotted lines), it is important to know the effects of these. We show in this section that long-range E-E connections are not able to stabilize the synchronous solution if that solution is unstable in the absence of those connections. Nevertheless, especially in the beta rhythm, they can be important in producing the appropriate network output by eliminating the possibility of other unwanted solutions.

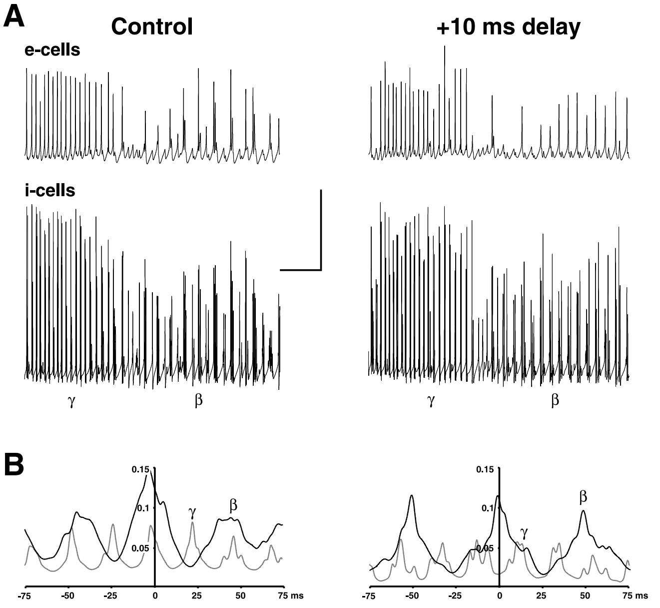

Fig. 4. In network model, beta remains synchronized with longer axonal delays than does gamma. The network consists of a 96 × 32 array of pyramidal cells (1.92 mm wide) and a superimposed 96 × 4 array of interneurons, as in ref. 14. In control conditions, the maximum axon conduction delay was 3.84 ms across the array. Oscillations were evoked by tonic depolarization of both pyramidal cells (E-cells) and interneurons (I-cells), with the gamma → beta transition occurring as pyramidal cell AHP conductances and excitatory postsynaptic potential conductances simultaneously increase (10, 18). In the case shown on the right, all axonal signals crossing the midline of the array were subjected to an additional 10-ms delay. (*A*) Gamma, followed by beta, as plotted in simultaneous traces of local average signals (224 nearby E-cells, 28 nearby I-cells). The E-cell signals appear similar, with and without the extra 10-ms delay. During beta, both E- and I-cell traces reveals an underlying oscillation at gamma frequency. (Bars = 20 mv, 200 ms.) (*B*) Cross-correlations of local average E-cell signals from opposite ends of the array, for 200 ms of gamma (thin lines) and 800 ms of beta (thick lines). In the control case, both gamma and beta have cross-correlation peaks within 3 ms of 0. With the extra 10-ms conduction delay, the gamma signal is almost anticorrelated between the two sites whereas the beta signal cross-correlation peak is at −1.4 ms.

Fig. 5*A* illustrates the key points. In the first part of Fig. 5*A*, we show the behavior of local circuits for the network in Fig. 3*A* (no dotted lines), with the parameters adjusted so that the local circuits are each oscillating in the gamma regime and the conduction delay is 13 ms. Note the lack of synchrony. With coupling between the E cells (add dotted lines), the circuits change behavior but do not synchronize, as shown in the second part. Thus, E-E connections do not overcome the inability of the gamma rhythm to synchronize in the presence of substantial delays. (This was true for all strengths of E-E coupling we tried.) The last portion of Fig. 5*A* shows that the system synchronizes if enough AHP current is added to the E-cells to slow down the local rhythm to beta.

To explain these results we make two points. First, we note that the E-E coupling does not significantly change the dynamics of the network when the cells are close to synchrony. The reason is that the conduction delay insures that the effect is felt after the spike of the cell postsynaptic to the excitatory postsynaptic potential, so is not felt on the current cycle. In addition, the excitatory postsynaptic potential (simulated as being AMPA receptor-mediated) decays fast enough so that the effect is negligible by the next cycle. Thus, with no AHP current, E-E coupling cannot change dynamics in which the synchronous state is unstable to dynamics that have synchrony as a stable state.

For the beta rhythm, E-E coupling is very important, as illustrated by Fig. 5*B*: The first portion shows the antiphase between the two sites that occur when each uncoupled site displays a beta

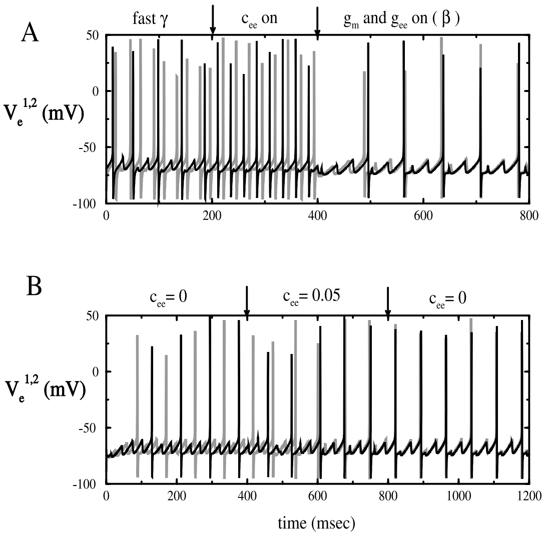

Fig. 5. (*A*) Fast gamma will not synchronize with a delay of 13 ms. If the long distance E-E coupling is turned on ($c_{ee} = 0.5$), synchrony still does not occur. However, if the AHP is then turned on ($g_m = 1$), the network shifts to a beta rhythm and synchronizes within two cycles. Parameters are as in the Appendix. Excitatory drive is 6 in one site and 6.5 in the other; inhibitory drive is 1.15 in both sites. The voltages of the two E-cells are represented by black and gray lines. (*B*) The main role played by the long-distance E-E connections is to prevent the anti-phase solution. For the first 400 ms, there is no long E-E connection. At $t = 400$, $c_{ee} = 0.05$, which induces synchrony within a few cycles. At $t = 400$, c_{ee} is reset to zero, but synchrony remains robust. Drives and AHP are as in A.

rhythm and the only long connections are E to I. Adding long E-E connections synchronizes the network. The last portion shows that this synchrony is maintained when the E-E connections are then removed, showing that network is bistable.

The role of the E-E coupling in Fig. 5*A* is not to stabilize synchrony, as shown above. Instead, the E-E coupling prevents the nonsynchronous solution that is shown in Fig. 5*B*. Near the solution shown in Fig. 5*B*, the effect of an excitatory postsynaptic potential on the postsynaptic E-cell can cause the latter to spike well before it would in the absence of E-E connections, preventing bistability.

Discussion

Modeling Issues. This paper addresses questions of behavior of large networks of neurons using small networks reduced to a minimal number of currents. The biophysical equations associated with those small networks still have on the order of 20 equations, far too many for an analytical approach. Thus, the map analyses that we presented represent a still further reduction of complexity. Nevertheless, the predictions that beta rhythms will synchronize at much larger delays than gamma was shown to hold for the very large, detailed, and realistic models. Indeed, the power of the mathematics we used was its ability to explain why any equations with the essential structural features (in our case, inhibition and an intrinsic AHP with the appropriate time constants) should lead to the observed outcomes.

The success of this method raises the question of why the very reduced descriptions are able to capture essential aspects of the network behavior: in particular, how the low dimensional maps can capture behavior of high dimensional differential equations. The key point we emphasize here is that the voltage-gated conductance equations have a large range of time scales associated with intrinsic and synaptic properties. The action potentials occur at (approximately) discrete times, initializing the time course of many of the currents; depending on the frequency of the rhythm, most of the fastest currents have stopped changing by the next discrete event. All of these fast events are lumped in the maps, leaving only the ones capable of transmitting phasic signals. Which processes are lumped together can change with alterations of parameters.

The simulations show that, for physiological parameter regimes, gamma rhythms support robust synchronization between sites for delays up to ≈8–10 ms. The beta rhythms (a subharmonic of gamma in the beta 1 range) support synchronization in our simulations for 20+ ms. The maps explain how this can be so and show that the ability to synchronize with long conduction delays depends on more than the frequency of the network: e.g., on the time scales of the currents participating in the rhythm. For example, simulations (not given) show that the faster the two-site (beat-skipping) beta, the more delay can be tolerated and still get synchronization; the analysis predicts this because, at higher frequencies, there is more of the AHP current left at the end of the cycle to provide a synchronization. Parameter ranges can also affect the outcome by changing the order of the spikes (excitatory and inhibitory) in the steady state configuration.

The architecture of the local and long connections also have effects that are not intuitive. For example, the local E-E connections are critical for producing beta at a single site (no internal delay). However, synchrony of the excitatory cells is possible between sites using E to I as the only long connections. The major role of the long E-E connections is to prevent a configuration in which the E-cells skip every other cycle, but with the two sites having E-cells in antiphase instead of synchrony. We note that E-E connections alone are not sufficient to produce synchrony between the E-cells (19, 20); that they are synchronizing in this case is attributable partly to the adaptation currents (21) and partly to the interaction with the inhibition in the network.

The analysis shows that coupling across distances lowers the frequency of the coupled rhythm. This was shown explicitly for the gamma rhythm (8, 11), and similar techniques provide a formula for the frequency of the beta rhythm. The lower frequency is attributable to two effects: First, the conduction delay itself lowers the frequency. Second, when there is synchronization across distances, there is an extra inhibitory spike associated with the extra excitation onto the I-cell; this extra inhibition slows down the next firing of the E-cells.

The addition of long-distance coupling can change the structure of the rhythm as well as the frequency. In particular, if two local circuits displaying the beta rhythm are coupled with a conduction delay, the resulting rhythm can have the structure of either a slow gamma rhythm (E cells and I cells have same frequency) or a beta rhythm (E cells skip beats); increasing the drive to the I-cells changes the coupled system from slow gamma to beta (simulation not shown.) The switch is accompanied by a drop in frequency, associated with the extra I-spike between pulses of the E-cells.

Connections to Experimental Observations. The induction of excitatory pyramidal cell firing as a subharmonic of a continuing gamma frequency subthreshold oscillation is a robust phenomenon in the hippocampus (10, 14) (Fig. 1*A*). Frequency analysis of oscillatory components of cortical EEG responses to visual or auditory sensory stimuli also reveals a similar pattern. An initial gamma response (evoked) switches to a beta response superimposed on which is a second gamma frequency component (C. Haenschel and J. Gruzelier, personal communication; ref. 15).

Further EEG studies have demonstrated that, in terms of coherence, the above type of beta oscillations are associated with temporal relationships between more spatially distant regions of the central nervous system than gamma oscillations. This suggests that the anatomically hierarchical pattern of processing sensory information (primary, supplementary sensory-associational areas) is mirrored by a hierarchical use of oscillation frequency used to bring about temporal correlations (7), at least within the gamma and beta bands.

Physical separation of areas of the central nervous system does not correlate well with axonal conduction delays between areas. For example, ipsilateral, intrahemispheric axon conduction velocities have been quoted to be as low as 1 mm/ms for longer collaterals (22), whereas interhemispheric, callosal axon conduction velocities appear to be 2–4 mm/ms, with some researchers observing callosal fiber conduction velocities of over 20 mm/ms (22). These estimates suggest that, at least for some conduction pathways, the conduction time between associational areas in the temporal and parietal lobes would be well over 10 ms.

However, conduction velocities for axonal projections in the central nervous system are plastic, changing in a use-dependent manner over time (23). Bilateral primary processing of sensory information is common, and synchronization at gamma frequencies across the corpus callosum has been seen for visual evoked response (24). The brain may therefore organize axonal connections between areas in the temporal domain (25). We suggest that the enhanced coherence afforded by beta frequency oscillations over gamma oscillations with long conduction delays may be used, in conjunction with modified signal velocities, to functionally delineate different interareal interactions involved in sensory processing.

Appendix

Simulations. Each site has two excitatory and one inhibitory neuron. Each excitatory neuron receives input from the local inhibitory neuron and all of the other excitatory neurons; each inhibitory neuron receives input from all of the excitatory neurons and also has self-inhibition. The units of conductance are mS/cm^2, those of current are μA/cm^2, and capacitance is μF/cm^2. The excitatory neurons satisfy equations of the form:

$$CV' = -0.1(V+67) - 100m^3h(V-50) - 80n^4(V+100) - g_{AHP}w(V+100) - I^e_{syn} + I^e_{appl} \qquad [5]$$

where the variables m, h, n, and w satisfy

$$m' = \frac{0.32(54+V)}{1-\exp(-(V+54)/4)}(1-m) - \frac{0.28(V+27)}{\exp((v+27)/5)-1}m,$$

$$h' = 0.128\exp(-(50+V)/18)(1-h) - \frac{4}{1+\exp(-(v+27)/5)}h,$$

$$n' = \frac{0.032(v+52)}{1-\exp(v+52)/5)}(1-n) - 0.5\exp(-(57+v)/40)n,$$

$$w' = \frac{w_\infty(V) - w}{\tau_w(V)},$$

where $w_\infty(V) = \dfrac{1}{1+\exp(-(V+35)/10)}$ and

$$\tau_w(V) = \frac{400}{3.3\exp((V+35)/20) + \exp(-(V+35)/20)}.$$

The inhibitory neurons have identical equations, but there is no AHP current. The capacitance is 1.

Synaptic currents are $I^e_{syn} = g_{ie}s_i(t)(V+80) + g_{ee}\bar{s}_e(t)V + c_{ee}\hat{s}_e(t-\delta)$ and $I^i_{syn} = [g_{ei}(s^1_e(t) + s^2_e(t)) + c_{ei}(\hat{s}^1_e(t-\delta) + \hat{s}^2_e(t-\delta)]V + g_{ii}\, s_i(t)(V+80)$. In all of the simulations, $g_{ie} = 1$, $g_{ei} = 0.15$, $g_{ii} = 0.2$, $g_{ee} = 0.15$, and $c_{ei} = 0.15$. The barred variables correspond to other excitatory cells in the same column, and the hatted correspond to other excitatory cells from the distant column. The synapses satisfy first order equations of the form: $s'_e = 5(1+\tanh(V/4))(1-s_e) - s_e/2$, $s'_i = 2(1+\tanh(V/4))(1-s_i) - s_i/15$. The current applied to the excitatory cells was between 5.5 and 7 and acted as the source for the heterogeneity between columns. The current applied to the inhibitory cells was 1.15. The main parameters that varied in the paper are the cross EE coupling, c_{ee} (0–0.05), the g_{AHP} (0–1.25), and the delay, δ.

The equations are integrated by using modified Euler with a step size of 0.025 ms because of the fact that the extrapolation used for the delay equations is only second order. The simulations were checked by using a smaller step size with no difference found. Code for the computations is available from G.B.E. in the form of an XPP file. XPP is a package for solving differential equations and is available at http://www.pitt.edu/~phase.

Computation of *D*. The plot of D in Fig. 3*C* is done by using Eq. **4** and the definitions of A and B. To do this, a formula must be derived for the maps T_I and T_β. Asymptotics suggests a form for the maps, and this formula was then hand-fitted to the numerical computations of the maps. The period of the oscillation scaled linearly with the delay. For Fig. 3*C*, $T_I(\delta) = 3.2/[1 - 1/(1 + 0.5(\delta + 0.2))]$, $T_\beta(\delta) = 34 + 12/(1 + 1.3\delta^2) - 0.13\delta$, and $p_\beta(\delta) = 60 + 0.7\delta$. In approximating the maps, we assume an exponential decay of the inhibitory synapses and the adaptation; this is not strictly correct because, in both cases, the equations are nonlinear. However, empirically, we can fit the parameters in Eqs. **2** and **4** by looking at the magnitudes of the variables, w (for the AHP) and s_i for the inhibition. We multiply these by their respective maximal conductances and then multiply that by $V_{rev} - \bar{V}$. Here, $\bar{V}$ is the mean potential of the cell, and V_{rev} is the reversal potential of the current. For the AHP it is -100 mV, and for the synapse it is -80 mV. The mean potential is -69 mV. Empirically, we find that $\tau_{AHP} = 50$, $\tau = 20$. From Eq. **4**, it is clear that, because the quantities A, B appear via a ratio, only the ratio $r = g^{eff}_{AHP}/g^{eff}_{ie}$ matters. Our empirical estimates of this are $R \approx 0.6$, based on the above approximations [the maximum that the synaptic gates get is ≈ 0.7, that of the AHP is ≈ 0.14, the maximal conductances are both ≈ 1, and $(-100 + 69)/(-80 + 69) \approx 3$ so that the ratio is ≈ 0.6]. With these three parameters τ, τ_{AHP}, and R, as well as the empirically determined functions $T_{\beta,I}(\delta)$, we can plot the function D. Note that, to plot D for the gamma rhythm, the period is not needed and neither is the decay of the inhibitory synapse; only the map T_I is required.

This work was partially supported by National Institutes of Health Grant R01 MH47150 to N.K. and G.B.E., grants from the National Science Foundation to N.K. and G.B.E. and grants from the Wellcome Trust to M.A.W. and R.D.T., who is a Wellcome Trust Principal Research Fellow.

1. Farmer, S. F. (1998) *J. Physiol.* **509,** 3–14.
2. Singer, W. (1993) *Annu. Rev. Physiol.* **55,** 349–374.
3. Traub, R. D., Jefferys, J. G. R. & Whittington, M. (1999) *Fast Oscillations in Cortical Circuits* (MIT Press, Cambridge, MA).
4. Bressler, Coppola, R. & Nakamura, R. (1993) *Nature (London)* **366,** 153–156.
5. Pantev, C. (1995) *Brain Topogr.* **7,** 321–330.
6. Roelfsema, P. R., Engel, A. K., König, P. & Singer, W. (1997) *Nature (London)* **385,** 157–161.
7. von Stein, A., Rappelsberger, P., Sarnthein, J. & Petsche, H. (1999) *Cereb. Cortex* **9,** 137- 150.
8. Traub, R. D., Whittington, M. A., Stanford, I. M. & Jefferys, J. G. R. (1996) *Nature (London)* **383,** 621–624.
9. Whittington, M. A., Stanford, I. M., Colling, S. B., Jefferys, J. G. R. & Traub, R. D. (1997) *J. Physiol.* **502,** 591–607.
10. Whittington, M. A., Traub, R. D., Faulkner, H,J., Stanford, I. M. & Jefferys, J. G. R. (1997) *Proc. Nat. Acad. Sci USA* **94,** 12198–12203.
11. Ermentrout, G. B. & Kopell, N. (1998) *Proc. Nat. Acad. Sci. USA* **95,** 1259–1264.
12. Karbowski, J. & Kopell, N. (2000) *Neural Comput.*, in press.
13. König, P. & Schillen, T. B. (1991) *Neural Comput.* **3,** 155–166.
14. Traub, R. D., Whittington, M. A., Buhl, E. H., Jefferys, J. G. R. & Faulkner, H. J. (1999) *J. Neurosci.* **3,** 1088–1105.
15. Tallon-Baudry, C., Bertrand, O., Delpuech, C. & Premier, J. (1998) *J. Neurosci.* **18,** 4244–4255.
16. Deuchars J. & Thomson, A. M. (1996) *Neuroscience* **74,** 1009–1018.
17. Traub, R. D., Whittington, M. A., Colling, S. B., Buzáski, G. B. & Jefferys, J. G. R. (1996) *J. Physiol.* **492,** 471–484.
18. Traub, R. D. & Miles, R. (1991) *Neuronal Networks of the Hippocampus* (Cambridge Univ. Press, Cambridge, U.K.).
19. Gerstner, W., van Hemmen, J. L. & Cowen, J. (1996) *Neural Comput.* **8,** 1653–1676.
20. van Vreeswijk, C., Abbott, L. F. & Ermentrout, G. B. (1994) *J. Comput. Neurosci.* **1,** 313–322.
21. Crook, S. M., Ermentrout, G. B. & Bower, J. M. (1998) *Neural Computation* **10,** 837–854.
22. Swadlow, H. A. (1990) *J. Neurophysiol.* **63,** 1477–1498.
23. Swadlow, H. A. (1985) *J. Neurophysiol.* **54,** 1346–1362.
24. Engel, A. K., Konig, P., Kreiter, A. K. & Singer, W. (1991) *Science* **252,** 1177–1179.
25. Sugihara, I., Lang, E. J. & Llinás, R. (1993) *J. Physiol.* **470,** 243–271.
26. Aroniadou, V. A. & Keller, A. (1993) *J. Neurophysiol.* **70,** 1553–1569.

The Journal of Physiology

A quantitative description of membrane current and its application to conduction and excitation in nerve

A. L. Hodgkin and A. F. Huxley

J. Physiol. 1952;117;500-544

This information is current as of January 29, 2008

The Journal of Physiology Online is the official journal of The Physiological Society. It has been published continuously since 1878. To subscribe to *The Journal of Physiology Online* go to: http://jp.physoc.org/subscriptions/. *The Journal of Physiology Online* articles are free 12 months after publication. No part of this article may be reproduced without the permission of Blackwell Publishing: JournalsRights@oxon.blackwellpublishing.com

Downloaded from jp.physoc.org by on January 29, 2008

This is the final published version of this article; it is available at:
http://jp.physoc.org

This version of the article may not be posted on a public website for 12 months after publication unless article is open access.

The Journal of Physiology Online is the official journal of The Physiological Society. It has been published continuously since 1878. To subscribe to *The Journal of Physiology Online* go to: http://jp.physoc.org/subscriptions/. *The Journal of Physiology Online* articles are free 12 months after publication. No part of this article may be reproduced without the permission of Blackwell Publishing: JournalsRights@oxon.blackwellpublishing.com

Downloaded from jp.physoc.org by on January 29, 2008

J. Physiol. (1952) 117, 500–544

A QUANTITATIVE DESCRIPTION OF MEMBRANE CURRENT AND ITS APPLICATION TO CONDUCTION AND EXCITATION IN NERVE

BY A. L. HODGKIN AND A. F. HUXLEY
From the Physiological Laboratory, University of Cambridge

(*Received* 10 *March* 1952)

This article concludes a series of papers concerned with the flow of electric current through the surface membrane of a giant nerve fibre (Hodgkin, Huxley & Katz, 1952; Hodgkin & Huxley, 1952*a–c*). Its general object is to discuss the results of the preceding papers (Part I), to put them into mathematical form (Part II) and to show that they will account for conduction and excitation in quantitative terms (Part III).

PART I. DISCUSSION OF EXPERIMENTAL RESULTS

The results described in the preceding papers suggest that the electrical behaviour of the membrane may be represented by the network shown in Fig. 1. Current can be carried through the membrane either by charging the membrane capacity or by movement of ions through the resistances in parallel with the capacity. The ionic current is divided into components carried by sodium and potassium ions (I_{Na} and I_{K}), and a small 'leakage current' (I_l) made up by chloride and other ions. Each component of the ionic current is determined by a driving force which may conveniently be measured as an electrical potential difference and a permeability coefficient which has the dimensions of a conductance. Thus the sodium current (I_{Na}) is equal to the sodium conductance (g_{Na}) multiplied by the difference between the membrane potential (E) and the equilibrium potential for the sodium ion (E_{Na}). Similar equations apply to I_{K} and I_l and are collected on p. 505.

Our experiments suggest that g_{Na} and g_{K} are functions of time and membrane potential, but that E_{Na}, E_{K}, E_l, C_M and $\bar{g}_l$ may be taken as constant. The influence of membrane potential on permeability can be summarized by stating: first, that depolarization causes a transient increase in sodium conductance and a slower but maintained increase in potassium conductance; secondly, that these changes are graded and that they can be reversed by repolarizing the membrane. In order to decide whether these effects are sufficient to account for complicated phenomena such as the action potential and refractory period, it is necessary to obtain expressions relating

Downloaded from jp.physoc.org by on January 29, 2008

the sodium and potassium conductances to time and membrane potential. Before attempting this we shall consider briefly what types of physical system are likely to be consistent with the observed changes in permeability.

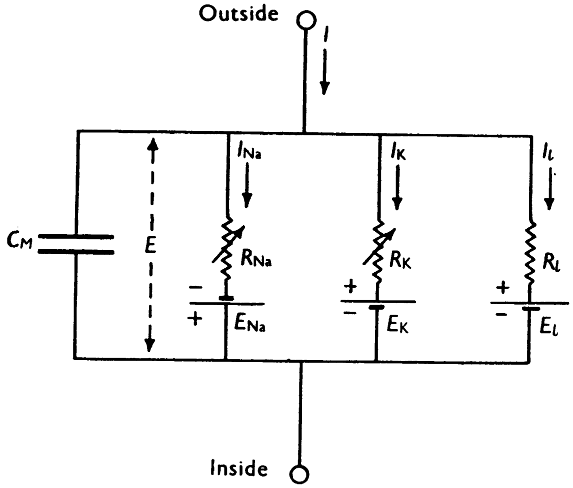

Fig. 1. Electrical circuit representing membrane. $R_{Na}=1/g_{Na}$; $R_K=1/g_K$; $R_l=1/\bar{g}_l$. R_{Na} and R_K vary with time and membrane potential; the other components are constant.

The nature of the permeability changes

At present the thickness and composition of the excitable membrane are unknown. Our experiments are therefore unlikely to give any certain information about the nature of the molecular events underlying changes in permeability. The object of this section is to show that certain types of theory are excluded by our experiments and that others are consistent with them.

The first point which emerges is that the changes in permeability appear to depend on membrane potential and not on membrane current. At a fixed depolarization the sodium current follows a time course whose form is independent of the current through the membrane. If the sodium concentration is such that $E_{Na} < E$, the sodium current is inward; if it is reduced until $E_{Na} > E$ the current changes in sign but still appears to follow the same time course. Further support for the view that membrane potential is the variable controlling permeability is provided by the observation that restoration of the normal membrane potential causes the sodium or potassium conductance to decline to a low value at any stage of the response.

The dependence of g_{Na} and g_K on membrane potential suggests that the permeability changes arise from the effect of the electric field on the distribution or orientation of molecules with a charge or dipole moment. By this we do not mean to exclude chemical reactions, for the rate at which these occur might depend on the position of a charged substrate or catalyst. All that is intended is that small changes in membrane potential would be most unlikely

Downloaded from jp.physoc.org by on January 29, 2008

to cause large alterations in the state of a membrane which was composed entirely of electrically neutral molecules.

The next question to consider is how changes in the distribution of a charged particle might affect the ease with which sodium ions cross the membrane. Here we can do little more than reject a suggestion which formed the original basis of our experiments (Hodgkin, Huxley & Katz, 1949). According to this view, sodium ions do not cross the membrane in ionic form but in combination with a lipoid soluble carrier which bears a large negative charge and which can combine with one sodium ion but no more. Since both combined and uncombined carrier molecules bear a negative charge they are attracted to the outside of the membrane in the resting state. Depolarization allows the carrier molecules to move, so that sodium current increases as the membrane potential is reduced. The steady state relation between sodium current and voltage could be calculated for this system and was found to agree reasonably with the observed curve at 0·2 msec after the onset of a sudden depolarization. This was encouraging, but the analogy breaks down if it is pursued further. In the model the first effect of depolarization is a movement of negatively charged molecules from the outside to the inside of the membrane. This gives an initial outward current, and an inward current does not occur until combined carriers lose sodium to the internal solution and return to the outside of the membrane. In our original treatment the initial outward current was reduced to vanishingly small proportions by assuming a low density of carriers and a high rate of movement and combination. Since we now know that the sodium current takes an appreciable time to reach its maximum, it is necessary to suppose that there are more carriers and that they react or move more slowly. This means that any inward current should be preceded by a large outward current. Our experiments show no sign of a component large enough to be consistent with the model. This invalidates the detailed mechanism assumed for the permeability change but it does not exclude the more general possibility that sodium ions cross the membrane in combination with a lipoid soluble carrier.

A different form of hypothesis is to suppose that sodium movement depends on the distribution of charged particles which do not act as carriers in the usual sense, but which allow sodium to pass through the membrane when they occupy particular sites in the membrane. On this view the rate of movement of the activating particles determines the rate at which the sodium conductance approaches its maximum but has little effect on the magnitude of the conductance. It is therefore reasonable to find that temperature has a large effect on the rate of rise of sodium conductance but a relatively small effect on its maximum value. In terms of this hypothesis one might explain the transient nature of the rise in sodium conductance by supposing that the activating particles undergo a chemical change after moving from the position which they occupy when the membrane potential is high. An alternative is to

Downloaded from jp.physoc.org by on January 29, 2008

attribute the decline of sodium conductance to the relatively slow movement of another particle which blocks the flow of sodium ions when it reaches a certain position in the membrane.

Much of what has been said about the changes in sodium permeability applies equally to the mechanism underlying the change in potassium permeability. In this case one might suppose that there is a completely separate system which differs from the sodium system in the following respects: (1) the activating molecules have an affinity for potassium but not for sodium; (2) they move more slowly; (3) they are not blocked or inactivated. An alternative hypothesis is that only one system is present but that its selectivity changes soon after the membrane is depolarized. A situation of this kind would arise if inactivation of the particles selective for sodium converted them into particles selective for potassium. However, this hypothesis cannot be applied in a simple form since the potassium conductance rises too slowly for a direct conversion from a state of sodium permeability to one of potassium permeability.

One of the most striking properties of the membrane is the extreme steepness of the relation between ionic conductance and membrane potential. Thus g_{Na} may be increased e-fold by a reduction of only 4 mV, while the corresponding figure for g_{K} is 5–6 mV (Hodgkin & Huxley, 1952*a*, figs. 9, 10). In order to illustrate the possible meaning of this result we shall suppose that a charged molecule which has some special affinity for sodium may rest either on the inside or the outside of the membrane but is present in negligible concentrations elsewhere. We shall also suppose that the sodium conductance is proportional to the number of such molecules on the inside of the membrane but is independent of the number on the outside. From Boltzmann's principle the proportion P_i of the molecules on the inside of the membrane is related to the proportion on the outside, P_o, by

$$\frac{P_i}{P_o} = \exp[(w + zeE)/kT],$$

where E is the potential difference between the outside and the inside of the membrane, w is the work required to move the molecule from the inside to the outside of the membrane when $E=0$, e is the absolute value of the electronic charge, z is the valency of the molecule (i.e. the number of positive electronic charges on it), k is Boltzmann's constant and T is the absolute temperature. Since we have assumed that $P_i + P_o = 1$ the expression for P_i is

$$P_i = 1 \bigg/ \left[1 + \exp - \left(\frac{w + zeE}{kT}\right)\right].$$

For negative values of z and with E sufficiently large and positive this gives

$$P_i = \text{constant} \times \exp[zeE/kT].$$

Downloaded from jp.physoc.org by on January 29, 2008

In order to explain our results z must be about -6 since $\frac{kT}{e}\left(=\frac{RT}{F}\right)$ is 25 mV at room temperature and $g_{Na} \propto \exp - E/4$ for E large. This suggests that the particle whose distribution changes must bear six negative electronic charges, or, if a similar theory is developed in terms of the orientation of a long molecule with a dipole moment, it must have at least three negative charges on one end and three positive charges on the other. A different but related approach is to suppose that sodium movement depends on the presence of six singly charged molecules at a particular site near the inside of the membrane. The proportion of the time that each of the charged molecules spends at the inside is determined by $\exp - E/25$ so that the proportion of sites at which all six are at the inside is $\exp - E/4{\cdot}17$. This suggestion may be given plausibility but not mathematical simplicity by imagining that a number of charges form a bridge or chain which allows sodium ions to flow through the membrane when it is depolarized. Details of the mechanism will probably not be settled for some time, but it seems difficult to escape the conclusion that the changes in ionic permeability depend on the movement of some component of the membrane which behaves as though it had a large charge or dipole moment. If such components exist it is necessary to suppose that their density is relatively low and that a number of sodium ions cross the membrane at a single active patch. Unless this were true one would expect the increase in sodium permeability to be accompanied by an outward current comparable in magnitude to the current carried by sodium ions. For movement of any charged particle in the membrane should contribute to the total current and the effect would be particularly marked with a molecule, or aggregate, bearing a large charge. As was mentioned earlier, there is no evidence from our experiments of any current associated with the change in sodium permeability, apart from the contribution of the sodium ion itself. We cannot set a definite upper limit to this hypothetical current, but it could hardly have been more than a few per cent of the maximum sodium current without producing a conspicuous effect at the sodium potential.

PART II. MATHEMATICAL DESCRIPTION OF MEMBRANE CURRENT DURING A VOLTAGE CLAMP

Total membrane current

The first step in our analysis is to divide the total membrane current into a capacity current and an ionic current. Thus

$$I = C_M \frac{\mathrm{d}V}{\mathrm{d}t} + I_i, \qquad (1)$$

Downloaded from jp.physoc.org by on January 29, 2008

where

I is the total membrane current density (inward current positive);
I_i is the ionic current density (inward current positive);
V is the displacement of the membrane potential from its resting value (depolarization negative);
C_M is the membrane capacity per unit area (assumed constant);
t is time.

The justification for this equation is that it is the simplest which can be used and that it gives values for the membrane capacity which are independent of the magnitude or sign of V and are little affected by the time course of V (see, for example, table 1 of Hodgkin *et al.* 1952). Evidence that the capacity current and ionic current are in parallel (as suggested by eqn. (1)) is provided by the similarity between ionic currents measured with $\frac{\mathrm{d}V}{\mathrm{d}t}=0$ and those calculated from $-C_M\frac{\mathrm{d}V}{\mathrm{d}t}$ with $I=0$ (Hodgkin *et al.* 1952).

The only major reservation which must be made about eqn. (1) is that it takes no account of dielectric loss in the membrane. There is no simple way of estimating the error introduced by this approximation, but it is not thought to be large since the time course of the capacitative surge was reasonably close to that calculated for a perfect condenser (Hodgkin *et al.* 1952).

The ionic current

A further subdivision of the membrane current can be made by splitting the ionic current into components carried by sodium ions (I_{Na}), potassium ions (I_{K}) and other ions (I_l):

$$I_i=I_{\mathrm{Na}}+I_{\mathrm{K}}+I_l. \tag{2}$$

The individual ionic currents

In the third paper of this series (Hodgkin & Huxley, 1952*b*), we showed that the ionic permeability of the membrane could be satisfactorily expressed in terms of ionic conductances (g_{Na}, g_{K} and $\bar{g}_l$). The individual ionic currents are obtained from these by the relations

$$I_{\mathrm{Na}}=g_{\mathrm{Na}}\,(E-E_{\mathrm{Na}}),$$
$$I_{\mathrm{K}}=g_{\mathrm{K}}\,(E-E_{\mathrm{K}}),$$
$$I_l=\bar{g}_l\,(E-E_l),$$

where E_{Na} and E_{K} are the equilibrium potentials for the sodium and potassium ions. E_l is the potential at which the 'leakage current' due to chloride and other ions is zero. For practical application it is convenient to write these equations in the form

$$I_{\mathrm{Na}}=g_{\mathrm{Na}}\,(V-V_{\mathrm{Na}}), \tag{3}$$
$$I_{\mathrm{K}}=g_{\mathrm{K}}\,(V-V_{\mathrm{K}}), \tag{4}$$
$$I_l=\bar{g}_l\,(V-V_l), \tag{5}$$

Downloaded from jp.physoc.org by on January 29, 2008

where

$$V = E - E_r,$$
$$V_{\mathrm{Na}} = E_{\mathrm{Na}} - E_r,$$
$$V_{\mathrm{K}} = E_{\mathrm{K}} - E_r,$$
$$V_l = E_l - E_r,$$

and E_r is the absolute value of the resting potential. V, V_{Na}, V_{K} and V_l can then be measured directly as displacements from the resting potential.

The ionic conductances

The discussion in Part I shows that there is little hope of calculating the time course of the sodium and potassium conductances from first principles. Our object here is to find equations which describe the conductances with reasonable accuracy and are sufficiently simple for theoretical calculation of the action potential and refractory period. For the sake of illustration we shall try to provide a physical basis for the equations, but must emphasize that the interpretation given is unlikely to provide a correct picture of the membrane.

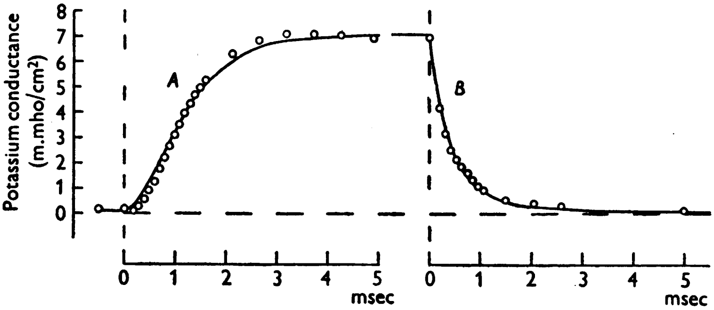

Fig. 2. A, rise of potassium conductance associated with depolarization of 25 mV; B, fall of potassium conductance associated with repolarization to the resting potential. Circles: experimental points replotted from Hodgkin & Huxley (1952*b*, Fig. 13). The last point of A is the same as the first point in B. Axon 18, 21° C in choline sea water. The smooth curve is drawn according to eqn. (11) with the following parameters:

	Curve A ($V = -25$ mV)	Curve B ($V = 0$)
$g_{\mathrm{K}0}$	0·09 m.mho/cm²	7·06 m.mho/cm²
$g_{\mathrm{K}\infty}$	7·06 m.mho/cm²	0·09 m.mho/cm²
τ_n	0·75 msec	1·1 msec

At the outset there is the difficulty that both sodium and potassium conductances increase with a delay when the axon is depolarized but fall with no appreciable inflexion when it is repolarized. This is illustrated by the circles in Fig. 2, which shows the change in potassium conductance associated with a depolarization of 25 mV lasting 4·9 msec. If g_{K} is used as a variable the end of the record can be fitted by a first-order equation but a third- or fourth-order equation is needed to describe the beginning. A useful simplification is

Downloaded from jp.physoc.org by on January 29, 2008

achieved by supposing that g_K is proportional to the fourth power of a variable which obeys a first-order equation. In this case the rise of potassium conductance from zero to a finite value is described by $(1-\exp(-t))^4$, while the fall is given by $\exp(-4t)$. The rise in conductance therefore shows a marked inflexion, while the fall is a simple exponential. A similar assumption using a cube instead of a fourth power describes the initial rise of sodium conductance, but a term representing inactivation must be included to cover the behaviour at long times.

The potassium conductance

The formal assumptions used to describe the potassium conductance are:

$$g_K = \bar{g}_K n^4, \tag{6}$$

$$\frac{dn}{dt} = \alpha_n (1-n) - \beta_n n, \tag{7}$$

where $\bar{g}_K$ is a constant with the dimensions of conductance/cm², α_n and β_n are rate constants which vary with voltage but not with time and have dimensions of $[\text{time}]^{-1}$, n is a dimensionless variable which can vary between 0 and 1.

These equations may be given a physical basis if we assume that potassium ions can only cross the membrane when four similar particles occupy a certain region of the membrane. n represents the proportion of the particles in a certain position (for example at the inside of the membrane) and $1-n$ represents the proportion that are somewhere else (for example at the outside of the membrane). α_n determines the rate of transfer from outside to inside, while β_n determines the transfer in the opposite direction. If the particle has a negative charge α_n should increase and β_n should decrease when the membrane is depolarized.

Application of these equations will be discussed in terms of the family of curves in Fig. 3. Here the circles are experimental observations of the rise of potassium conductance associated with depolarization, while the smooth curves are theoretical solutions of eqns. (6) and (7).

In the resting state, defined by $V=0$, n has a resting value given by

$$n_0 = \frac{\alpha_{n0}}{\alpha_{n0} + \beta_{n0}}.$$

If V is changed suddenly α_n and β_n instantly take up values appropriate to the new voltage. The solution of (7) which satisfies the boundary condition that $n = n_0$ when $t = 0$ is

$$n = n_\infty - (n_\infty - n_0) \exp(-t/\tau_n), \tag{8}$$

where

$$n_\infty = \alpha_n/(\alpha_n + \beta_n), \tag{9}$$

and

$$\tau_n = 1/(\alpha_n + \beta_n). \tag{10}$$

Downloaded from jp.physoc.org by on January 29, 2008

From eqn. (6) this may be transformed into a form suitable for comparison with the experimental results, i.e.

$$g_K = \{(g_{K\infty})^{\frac{1}{4}} - [(g_{K\infty})^{\frac{1}{4}} - (g_{K0})^{\frac{1}{4}}] \exp(-t/\tau_n)\}^4, \tag{11}$$

where $g_{K\infty}$ is the value which the conductance finally attains and g_{K0} is the conductance at $t=0$. The smooth curves in Fig. 3 were calculated from

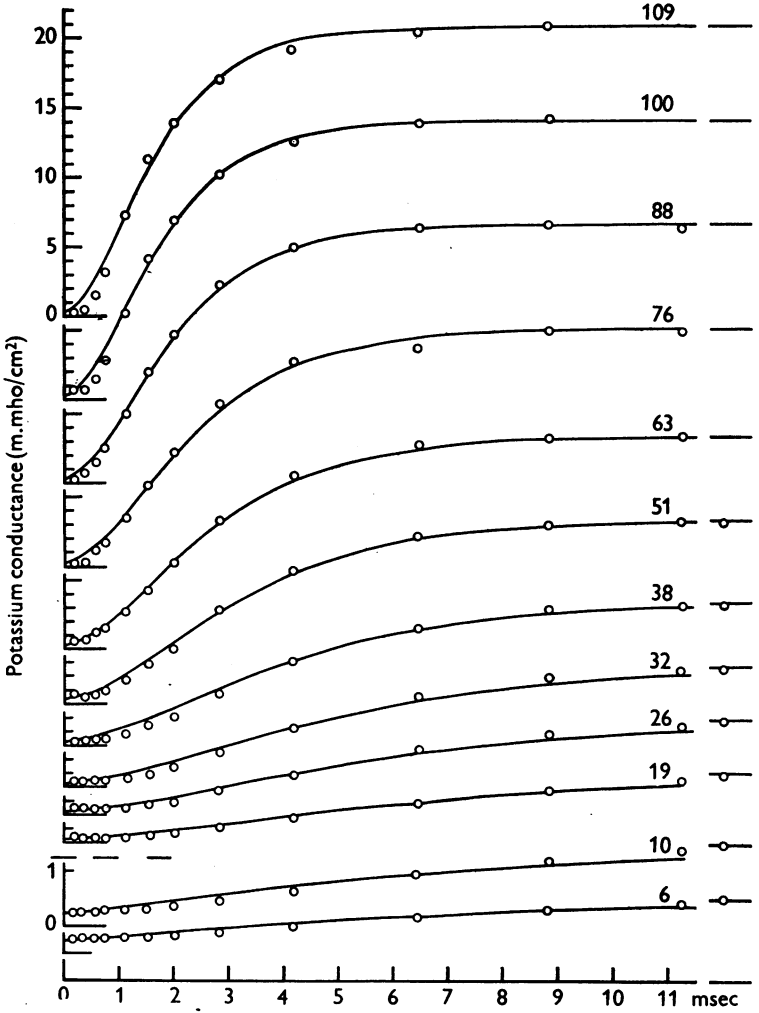

Fig. 3. Rise of potassium conductance associated with different depolarizations. The circles are experimental points obtained on axon 17, temperature 6–7° C, using observations in sea water and choline sea water (see Hodgkin & Huxley, 1952*a*). The smooth curves were drawn from eqn. (11) with $g_{K0} = 0{\cdot}24$ m.mho/cm² and other parameters as shown in Table 1. The time scale applies to all records. The ordinate scale is the same in the upper ten curves (*A* to *J*) and is increased fourfold in the lower two curves (*K* and *L*). The number on each curve gives the depolarization in mV.

Downloaded from jp.physoc.org by on January 29, 2008

eqn. (11) with a value of τ_n chosen to give the best fit. It will be seen that there is reasonable agreement between theoretical and experimental curves, except that the latter show more initial delay. Better agreement might have been obtained with a fifth or sixth power, but the improvement was not considered to be worth the additional complication.

The rate constants α_n *and* β_n. At large depolarizations $g_{K\infty}$ seems to approach an asymptote about 20–50% greater than the conductance at -100 mV.

TABLE 1. Analysis of curves in Fig. 3

Curve	V (mV) (1)	$g_{K\infty}$ (m.mho/cm^2) (2)	n_∞ (3)	τ_n (msec) (4)	α_n (msec^{-1}) (5)	β_n (msec^{-1}) (6)
—	$(-\infty)$	(24·31)	(1·000)	—	—	—
A	-109	20·70	0·961	1·05	0·915	0·037
B	-100	20·00	0·953	1·10	0·866	0·043
C	-88	18·60	0·935	1·25	0·748	0·052
D	-76	17·00	0·915	1·50	0·610	0·057
E	-63	15·30	0·891	1·70	0·524	0·064
F	-51	13·27	0·859	2·05	0·419	0·069
G	-38	10·29	0·806	2·60	0·310	0·075
H	-32	8·62	0·772	3·20	0·241	0·071
I	-26	6·84	0·728	3·80	0·192	0·072
J	-19	5·00	0·674	4·50	0·150	0·072
K	-10	1·47	0·496	5·25	0·095	0·096
L	-6	0·98	0·448	5·25	0·085	0·105
—	(0)	(0·24)	(0·315)	—	—	—

Col. 1 shows depolarization in mV; col. 2, final potassium conductance; col. 3, $n_\infty = (g_{K\infty}/\bar{g}_K)^{\frac{1}{4}}$; col. 4, time constant used to compute curve; col. 5, $\alpha_n = n_\infty/\tau_n$; col. 6, $\beta_n = (1 - n_\infty)/\tau_n$. The figure of 24·31 was chosen for $\bar{g}_K$ because it made the asymptotic value of n_∞ 5% greater than the value at -100 mV.

For the purpose of calculation we assume that $n = 1$ at the asymptote which is taken as about 20% greater than the value of $g_{K\infty}$ at $V = -100$ mV. These assumptions are somewhat arbitrary, but should introduce little error since we are not concerned with the behaviour of g_K at depolarizations greater than about 110 mV. In the experiment illustrated by Fig. 3, $g_{K\infty} = 20$ m.mho/cm^2 at $V = -100$ mV. $\bar{g}_K$ was therefore chosen to be near 24 m.mho/cm^2. This value was used to calculate n_∞ at various voltages by means of eqn. (6). α_n and β_n could then be obtained from the following relations which are derived from eqns. (9) and (10):

$$\alpha_n = n_\infty/\tau_n,$$

$$\beta_n = (1 - n_\infty)/\tau_n.$$

The results of analysing the curves in Fig. 3 by this method are shown in Table 1.

An estimate of the resting values of α_n and β_n could be obtained from the decline in potassium conductance associated with repolarization. The procedure was essentially the same but the results were approximate because the

Downloaded from jp.physoc.org by on January 29, 2008

resting value of the potassium conductance was not known with any accuracy when the membrane potential was high. Fig. 2 illustrates an experiment in which the membrane potential was restored to its resting value after a depolarization of 25 mV. It will be seen that both the rise and fall of the potassium conductance agree reasonably with theoretical curves calculated from eqn. (11) after an appropriate choice of parameters. The rate constants derived from these parameters were (in msec^{-1}): $\alpha_n = 0{\cdot}21$, $\beta_n = 0{\cdot}70$ when $V = 0$ and $\alpha_n = 0{\cdot}90$, $\beta_n = 0{\cdot}43$ when $V = -25$ mV.

In order to find functions connecting α_n and β_n with membrane potential we collected all our measurements and plotted them against V, as in Fig. 4. Differences in temperature were allowed for by adopting a temperature coefficient of 3 (Hodgkin *et al.* 1952) and scaling to 6° C. The effect of replacing sodium by choline on the resting potential was taken into account by displacing the origin for values in choline sea water by +4 mV. The continuous curves, which are clearly a good fit to the experimental data, were calculated from the following expressions:

$$\alpha_n = 0{\cdot}01\,(V+10) \Big/ \left[\exp\frac{V+10}{10} - 1\right], \qquad (12)$$

$$\beta_n = 0{\cdot}125\,\exp\,(V/80), \qquad (13)$$

where α_n and β_n are given in reciprocal msec and V is the displacement of the membrane potential from its resting value in mV.

These expressions should also give a satisfactory formula for the steady potassium conductance ($g_{K\infty}$) at any membrane potential (V), for this relation is implicit in the measurement of α_n and β_n. This is illustrated by Fig. 5, in which the abscissa is the membrane potential and the ordinate is $(g_{K\infty}/\bar{g}_K)^{\frac{1}{4}}$. The smooth curve was calculated from eqn. (9) with α_n and β_n substituted from eqns. (12) and (13).

Fig. 4 shows that β_n is small compared to α_n over most of the range; we therefore do not attach much weight to the curve relating β_n to V and have used the simplest expression which gave a reasonable fit. The function for α_n was chosen for two reasons. First, it is one of the simplest which fits the experimental results and, secondly, it bears a close resemblance to the equation derived by Goldman (1943) for the movements of a charged particle in a constant field. Our equations can therefore be given a qualitative physical basis if it is supposed that the variation of α and β with membrane potential arises from the effect of the electric field on the movement of a negatively charged particle which rests on the outside of the membrane when V is large and positive, and on the inside when it is large and negative. The analogy cannot be pressed since α and β are not symmetrical about $E = 0$, as they should be if Goldman's theory held in a simple form. Better agreement might

Downloaded from jp.physoc.org by on January 29, 2008

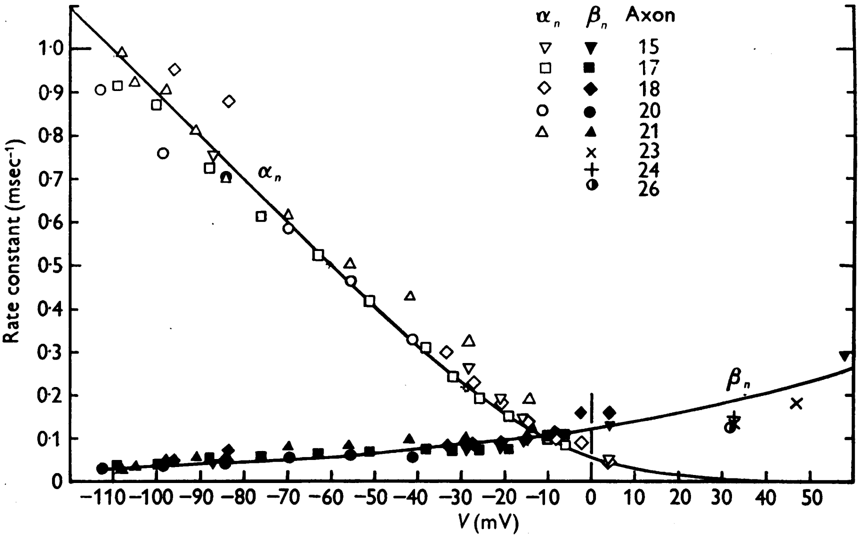

Fig. 4. Abscissa: membrane potential minus resting potential in sea water. Ordinate: rate constants determining rise (α_n) or fall (β_n) of potassium conductance at 6° C. The resting potential was assumed to be 4 mV higher in choline sea water than in ordinary sea water. Temperature differences were allowed for by assuming a Q_{10} of 3. All values for $V < 0$ were obtained by the method illustrated by Fig. 3 and Table 1; those for $V > 0$ were obtained from the decline of potassium conductance associated with an increase of membrane potential or from repolarization to the resting potential in choline sea water (e.g. Fig. 2). Axons 17–21 at 6–11° C, the remainder at about 20° C. The smooth curves were drawn from eqns. (12) and (13).

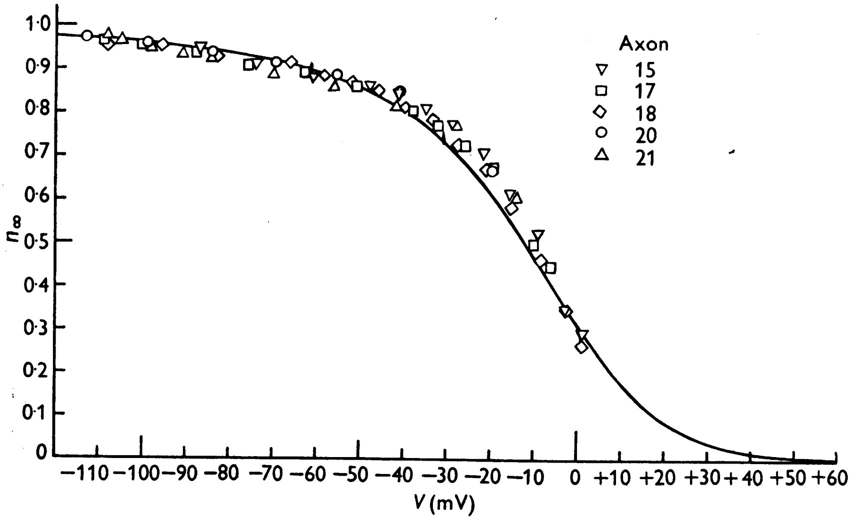

Fig. 5. Abscissa: membrane potential minus resting potential in sea water. Ordinate: experimental measurements of n_∞ calculated from the steady potassium conductance by the relation $n_\infty = \sqrt[4]{(g_{K\infty}/\bar{g}_K)}$, where $\bar{g}_K$ is the 'maximum' potassium conductance. The smooth curve is drawn according to eqn. (9).

Downloaded from jp.physoc.org by on January 29, 2008

be obtained by postulating some asymmetry in the structure of the membrane, but this assumption was regarded as too speculative for profitable consideration.

The sodium conductance

There are at least two general methods of describing the transient changes in sodium conductance. First, we might assume that the sodium conductance is determined by a variable which obeys a second-order differential equation. Secondly, we might suppose that it is determined by two variables, each of which obeys a first-order equation. These two alternatives correspond roughly to the two general types of mechanism mentioned in connexion with the nature of inactivation (pp. 502–503). The second alternative was chosen since it was simpler to apply to the experimental results.

The formal assumptions made are:

$$g_{\mathrm{Na}} = m^3 h \bar{g}_{\mathrm{Na}}, \tag{14}$$

$$\frac{\mathrm{d}m}{\mathrm{d}t} = \alpha_m (1-m) - \beta_m m, \tag{15}$$

$$\frac{\mathrm{d}h}{\mathrm{d}t} = \alpha_h (1-h) - \beta_h h, \tag{16}$$

where $\bar{g}_{\mathrm{Na}}$ is a constant and the α's and β's are functions of V but not of t.

These equations may be given a physical basis if sodium conductance is assumed to be proportional to the number of sites on the inside of the membrane which are occupied simultaneously by three activating molecules but are not blocked by an inactivating molecule. m then represents the proportion of activating molecules on the inside and $1-m$ the proportion on the outside; h is the proportion of inactivating molecules on the outside and $1-h$ the proportion on the inside. α_m or β_h and β_m or α_h represent the transfer rate constants in the two directions.

Application of these equations will be discussed first in terms of the family of curves in Fig. 6. Here the circles are experimental estimates of the rise and fall of sodium conductance during a voltage clamp, while the smooth curves were calculated from eqns. (14)–(16).

The solutions of eqns. (15) and (16) which satisfy the boundary conditions $m = m_0$ and $h = h_0$ at $t = 0$ are

$$m = m_\infty - (m_\infty - m_0) \exp(-t/\tau_m), \tag{17}$$

$$h = h_\infty - (h_\infty - h_0) \exp(-t/\tau_h), \tag{18}$$

where $m_\infty = \alpha_m/(\alpha_m + \beta_m)$ and $\tau_m = 1/(\alpha_m + \beta_m)$,

$h_\infty = \alpha_h/(\alpha_h + \beta_h)$ and $\tau_h = 1/(\alpha_h + \beta_h)$.

In the resting state the sodium conductance is very small compared with the value attained during a large depolarization. We therefore neglect m_0 if the

Downloaded from jp.physoc.org by on January 29, 2008

depolarization is greater than 30 mV. Further, inactivation is very nearly complete if $V < -30$ mV so that h_∞ may also be neglected. The expression for the sodium conductance then becomes

$$g_{\mathrm{Na}} = g'_{\mathrm{Na}} \left[1 - \exp\left(-t/\tau_m\right)\right]^3 \exp\left(-t/\tau_h\right), \tag{19}$$

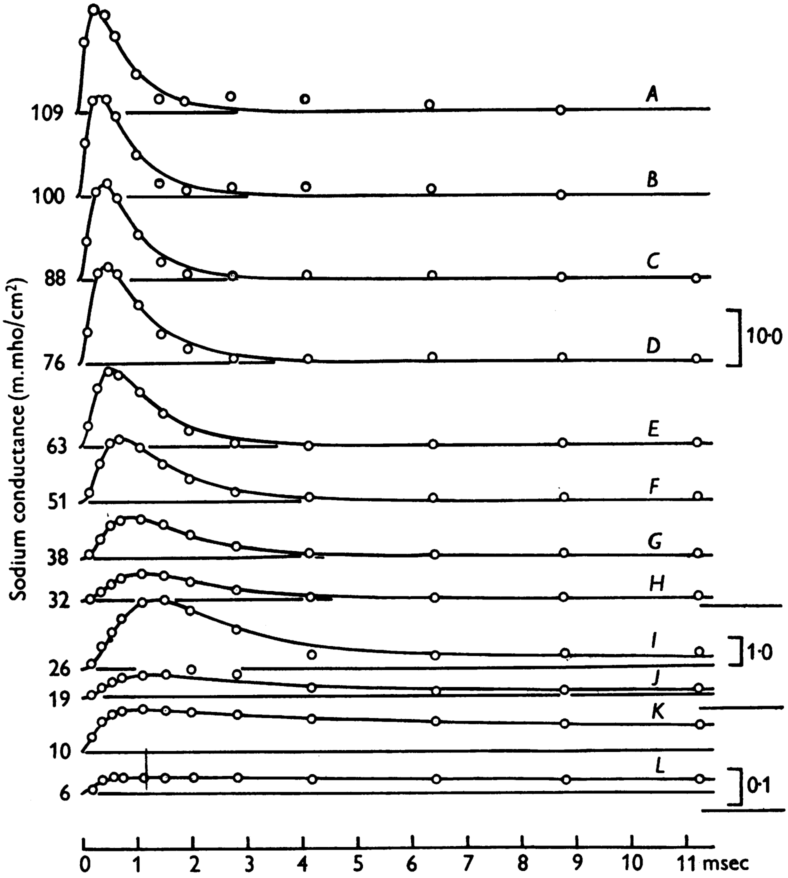

Fig. 6. Changes of sodium conductance associated with different depolarizations. The circles are experimental estimates of sodium conductance obtained on axon 17, temperature 6–7° C (cf. Fig. 3). The smooth curves are theoretical curves with parameters shown in Table 2; A to H drawn from eqn. 19, I to L from 14, 17, 18 with $\bar{g}_{\mathrm{Na}} = 70{\cdot}7$ m.mho/cm². The ordinate scales on the right are given in m.mho/cm². The numbers on the left show the depolarization in mV. The time scale applies to all curves.

where $g'_{\mathrm{Na}} = \bar{g}_{\mathrm{Na}} m_\infty^3 h_0$ and is the value which the sodium conductance would attain if h remained at its resting level (h_0). Eqn. (19) was fitted to an experimental curve by plotting the latter on double log paper and comparing it with a similar plot of a family of theoretical curves drawn with different ratios of τ_m to τ_h. Curves A to H in Fig. 6 were obtained by this method and gave the

Downloaded from jp.physoc.org by on January 29, 2008

TABLE 2. Analysis of curves in Fig. 6

Curve	V (mV)	g'_{Na} (m.mho/cm^2)	m_∞	τ_m (msec)	α_m (msec^{-1})	β_m (msec^{-1})	τ_h (msec)	h_∞	α_h (msec^{-1})	β_h (msec^{-1})
—	($-\infty$)	(42·9)	(1·00)	—	—	—	—	—	—	—
A	−109	40·3	0·980	0·140	7·0	(0·14)	0·67	(0)	(0)	1·50
B	−100	42·6	0·997	0·160	6·2	(0·02)	0·67	(0)	(0)	1·50
C	− 88	46·8	1·029	0·200	5·15	(−0·14)	0·67	(0)	(0)	1·50
D	− 76	39·5	0·975	0·189	5·15	0·13	0·84	(0)	(0)	1·19
E	− 63	38·2	0·963	0·252	3·82	0·15	0·84	(0)	(0)	1·19
F	− 51	30·7	0·895	0·318	2·82	0·33	1·06	(0)	(0)	0·94
G	− 38	20·0	0·778	0·382	2·03	0·58	1·27	(0)	(0)	0·79
H	− 32	15·3	0·709	0·520	1·36	0·56	1·33	(0)	(0)	0·75
I	− 26	7·90	0·569	0·600	0·95	0·72	(1·50)	(0·029)	(0·02)	(0·65)
J	− 19	1·44	0·323	0·400	0·81	1·69	(2·30)	(0·069)	(0·03)	(0·40)
K	− 10	0·13	0·145	0·220	0·66	3·9	(5·52)	(0·263)	(0·05)	(0·13)
L	− 6	0·046	0·103	0·200	0·51	4·5	(6·73)	(0·388)	(0·06)	(0·09)
—	(0)	(0·0033)	(0·042)	—	—	—	—	(0·608)	—	—

Values enclosed in brackets were not plotted in Figs. 7–10 either because they were too small to be reliable or because they were not independent measurements obtained in this experiment.

Downloaded from jp.physoc.org by on January 29, 2008

values of g'_{Na}, τ_m and τ_h shown in Table 2. Curves *I* to *L* were obtained from eqns. (17) and (18) assuming that h_∞ and τ_h had values calculated from experiments described in a previous paper (Hodgkin & Huxley, 1952 *c*).

The rate constants α_m and β_m. Having fitted theoretical curves to the experimental points, α_m and β_m were found by a procedure similar to that used with α_n and β_n, i.e.

$$\alpha_m = m_\infty/\tau_m, \quad \beta_m = (1 - m_\infty)/\tau_m,$$

the value of m_∞ being obtained from $\sqrt[3]{g'_{\mathrm{Na}}}$ on the basis that m_∞ approaches unity at large depolarizations.

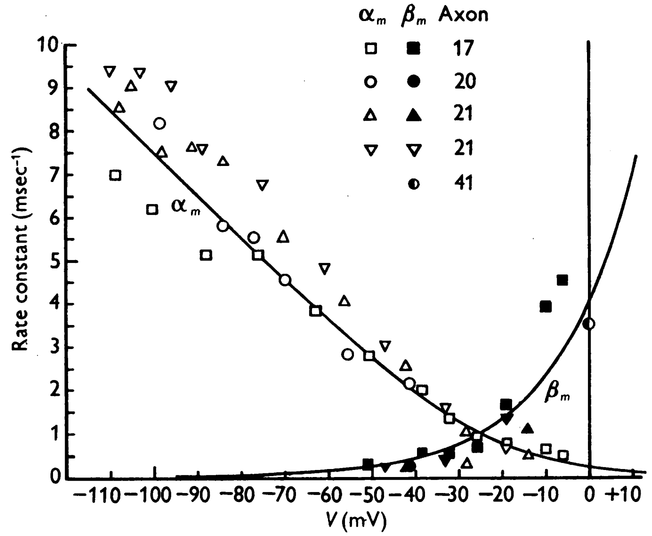

Fig. 7. Abscissa: membrane potential minus resting potential in sea water. Ordinate: rate constants (α_m and β_m) determining initial changes in sodium conductance at 6° C. All values for $V<0$ were obtained by the method illustrated by Fig. 6 and Table 2; the value at $V=0$ was obtained from the decline in sodium conductance associated with repolarization to the resting potential. The temperature varied between 3 and 11° C and was allowed for by assuming a Q_{10} of 3. The smooth curves were drawn from eqns. (20) and (21).

Values of α_m and β_m were collected from different experiments, reduced to a temperature of 6° C by adopting a Q_{10} of 3 and plotted in the manner shown in Fig. 7. The point for $V=0$ was obtained from what we regard as the most reliable estimate of the rate constant determining the decline of sodium conductance when the membrane is repolarized (Hodgkin & Huxley, 1952*b*, table 1, axon 41). The smooth curves in Fig. 7 were drawn according to the equations:

$$\alpha_m = 0{\cdot}1\ (V+25)\Big/\left(\exp\frac{V+25}{10}-1\right), \tag{20}$$

$$\beta_m = 4\ \exp\ (V/18), \tag{21}$$

where α_m and β_m are expressed in msec^{-1} and V is in mV.

Downloaded from jp.physoc.org by on January 29, 2008

Fig. 8 illustrates the relation between m_∞ and V. The symbols are experimental estimates and the smooth curve was calculated from the equation

$$m_\infty = \alpha_m/(\alpha_m + \beta_m), \tag{22}$$

where α_m and β_m have the values given by eqns. (20) and (21).

The rate constants α_h and β_h. The rate constants for the inactivation process were calculated from the expressions

$$\alpha_h = h_\infty/\tau_h,$$
$$\beta_h = (1 - h_\infty)/\tau_h.$$

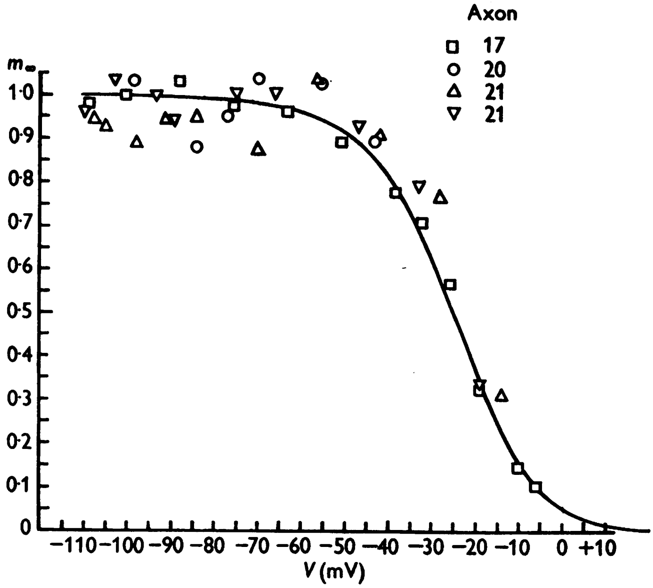

Fig. 8. Abscissa: membrane potential minus resting potential in sea water. Ordinate: m_∞ obtained by fitting curves to observed changes in sodium conductance at different depolarizations (e.g. Fig. 6 and Table 2). The smooth curve is drawn according to eqn. (22). The experimental points are proportional to the cube root of the sodium conductance which would have been obtained if there were no inactivation.

Values obtained by these equations are plotted against membrane potential in Fig. 9. The points for $V < -30$ mV were derived from the analysis described in this paper (e.g. Table 2), while those for $V > -30$ mV were obtained from the results given in a previous paper (Hodgkin & Huxley, 1952 *c*). A temperature coefficient of 3 was assumed and differences in resting potential were allowed for by taking the origin at a potential corresponding to $h_\infty = 0{\cdot}6$.

The smooth curves in this figure were calculated from the expressions

$$\alpha_h = 0{\cdot}07 \exp(V/20), \tag{23}$$

and

$$\beta_h = 1\bigg/\left(\exp\frac{V+30}{10} + 1\right). \tag{24}$$

Downloaded from jp.physoc.org by on January 29, 2008

The steady state relation between h_∞ and V is shown in Fig. 10. The smooth curve is calculated from the relation

$$h_\infty = \alpha_h/(\alpha_h + \beta_h), \tag{25}$$

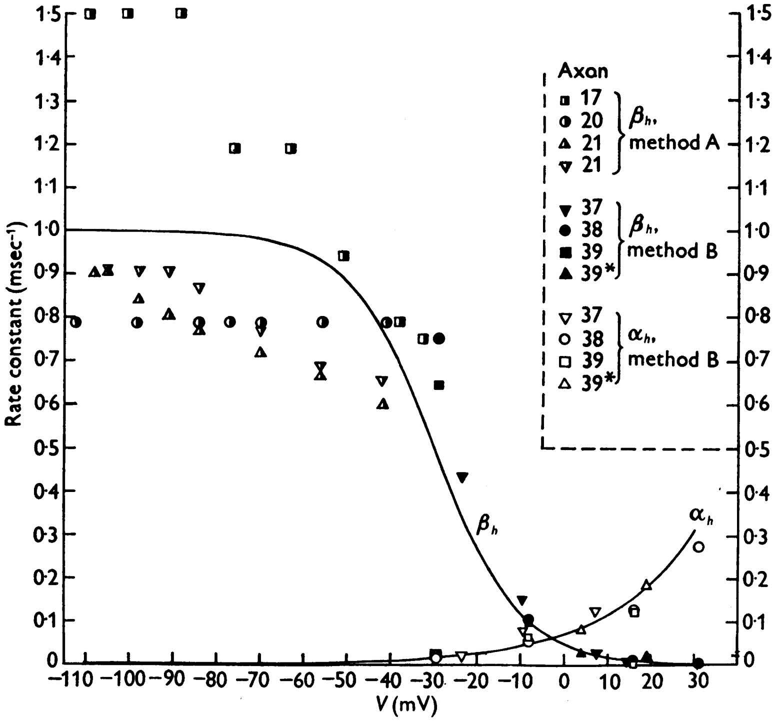

Fig. 9. Rate constants of inactivation (α_h and β_h) as functions of membrane potential (V). The smooth curves were calculated from eqns. (23) and (24). The experimental values of α_h and β_h were obtained from data such as those in Table 2 of this paper (method A) or from the values of τ_h and h_∞ given in Table 1 of Hodgkin & Huxley (1952c) (method B). Temperature differences were allowed for by scaling with a Q_{10} of 3. Axon 39 was at 19° C; all others at 3–9° C. The values for axons 37 and 39* were displaced by −1·5 and −12 mV in order to give $h_\infty = 0{\cdot}6$ at $V = 0$.

with α_h and β_h given by eqns. (23) and (24). If $V > -30$ mV this expression approximates to the simple expression used in a previous paper (Hodgkin & Huxley, 1952 c), i.e.

$$h_\infty = 1\bigg/\left(1 + \exp\frac{V_h - V}{7}\right),$$

where V_h is about −2 and is the potential at which $h_\infty = 0{\cdot}5$. This equation is the same as that giving the effect of a potential difference on the proportion of negatively charged particles on the outside of a membrane to the total number of such particles on both sides of the membrane (see p. 503). It is therefore consistent with the suggestion that inactivation might be due to the

Downloaded from jp.physoc.org by on January 29, 2008

movement of a negatively charged particle which blocks the flow of sodium ions when it reaches the inside of the membrane. This is encouraging, but it must be mentioned that a physical theory of this kind does not lead to satisfactory functions for α_h and β_h without further *ad hoc* assumptions.

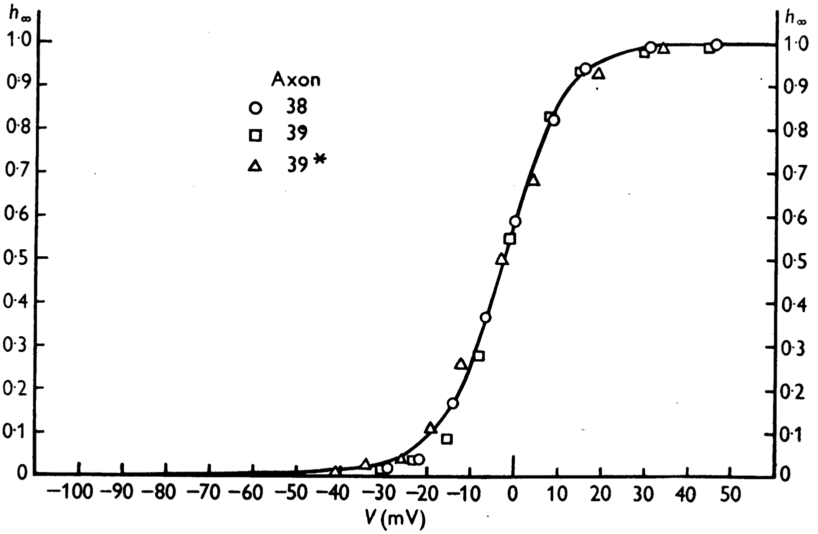

Fig. 10. Steady state relation between h and V. The smooth curve is drawn according to eqn. (25). The experimental points are those given in Table 1 of Hodgkin & Huxley (1952*c*). Axon 38 (5° C) as measured. Axon 39 (19° C) displaced −1·5 mV. Axon 39* (3° C, fibre in derelict state) displaced −12 mV. The curve gives the fraction of the sodium-carrying system which is readily available, as a function of membrane potential, in the steady state.

PART III. RECONSTRUCTION OF NERVE BEHAVIOUR

The remainder of this paper will be devoted to calculations of the electrical behaviour of a model nerve whose properties are defined by the equations which were fitted in Part II to the voltage clamp records described in the earlier papers of this series.

Summary of equations and parameters

We may first collect the equations which give the total membrane current I as a function of time and voltage. These are:

$$I = C_M \frac{\mathrm{d}V}{\mathrm{d}t} + \bar{g}_\mathrm{K} n^4 (V - V_\mathrm{K}) + \bar{g}_\mathrm{Na} m^3 h (V - V_\mathrm{Na}) + \bar{g}_l (V - V_l), \tag{26}$$

where

$$\mathrm{d}n/\mathrm{d}t = \alpha_n(1-n) - \beta_n n, \tag{7}$$

$$\mathrm{d}m/\mathrm{d}t = \alpha_m(1-m) - \beta_m m, \tag{15}$$

$$\mathrm{d}h/\mathrm{d}t = \alpha_h(1-h) - \beta_h h, \tag{16}$$

Downloaded from jp.physoc.org by on January 29, 2008

and
$$\alpha_n = 0{\cdot}01\ (V+10) \Big/ \left(\exp\frac{V+10}{10} - 1\right), \tag{12}$$

$$\beta_n = 0{\cdot}125 \exp\,(V/80), \tag{13}$$

$$\alpha_m = 0{\cdot}1\ (V+25) \Big/ \left(\exp\frac{V+25}{10} - 1\right), \tag{20}$$

$$\beta_m = 4 \exp\,(V/18), \tag{21}$$

$$\alpha_h = 0{\cdot}07 \exp\,(V/20), \tag{23}$$

$$\beta_h = 1 \Big/ \left(\exp\frac{V+30}{10} + 1\right). \tag{24}$$

Equation (26) is derived simply from eqns. (1)–(6) and (14) in Part II. The four terms on the right-hand side give respectively the capacity current, the current carried by K ions, the current carried by Na ions and the leak current, for 1 cm^2 of membrane. These four components are in parallel and add up to give the total current density through the membrane I. The conductances to K and Na are given by the constants $\bar{g}_K$ and $\bar{g}_{Na}$, together with the dimensionless quantities n, m and h, whose variation with time after a change of membrane potential is determined by the three subsidiary equations (7), (15) and (16). The α's and β's in these equations depend only on the instantaneous value of the membrane potential, and are given by the remaining six equations.

Potentials are given in mV, current density in μA/cm^2, conductances in m.mho/cm^2, capacity in μF/cm^2, and time in msec. The expressions for the α's and β's are appropriate to a temperature of 6·3° C; for other temperatures they must be scaled with a Q_{10} of 3.

The constants in eqn. (26) are taken as independent of temperature. The values chosen are given in Table 3, column 2, and may be compared with the experimental values in columns 3 and 4.

Membrane currents during a voltage clamp

Before applying eqn. (26) to the action potential it is well to check that it predicts correctly the total current during a voltage clamp. At constant voltage $\mathrm{d}V/\mathrm{d}t = 0$ and the coefficients α and β are constant. The solution is then obtained directly in terms of the expressions already given for n, m and h (eqns. (8), (17) and (18)). The total ionic current was computed from these for a number of different voltages and is compared with a series of experimental curves in Fig. 11. The only important difference is that the theoretical current has too little delay at the sodium potential; this reflects the inability of our equations to account fully for the delay in the rise of g_K (p. 509).

'Membrane' and propagated action potentials

By a 'membrane' action potential is meant one in which the membrane potential is uniform, at each instant, over the whole of the length of fibre

Downloaded from jp.physoc.org by on January 29, 2008

TABLE 3

Constant (1)	Value chosen (2)	Experimental values: Mean (3)	Experimental values: Range (4)	Reference (5)
C_M (μF/cm^2)	1·0	0·91	0·8 to 1·5	Table 1, Hodgkin *et al.* (1952)
V_{Na} (mV)	-115	-109	-95 to -119	p. 455, Hodgkin & Huxley (1952*a*)
V_K (mV)	$+12$	$+11$	$+9$ to $+14$	Table 3, values for low temperature in sea water, Hodgkin & Huxley (1952*b*)
V_l (mV)	$-10·613$*	-11	-4 to -22	Table 5, Hodgkin & Huxley (1952*b*)
$\bar{g}_{Na}$ (m.mho/cm^2)	120	80	65 to 90	Fully analysed results, Table 2† Hodgkin & Huxley (1952*a*)
		160	120 to 260	Fresh fibres, p. 465†
$\bar{g}_K$ (m.mho/cm^2)	36	34	26 to 49	p. 463, Hodgkin & Huxley (1952*a*)
$\bar{g}_l$ (m.mho/cm^2)	0·3	0·26	0·13 to 0·50	Table 5, Hodgkin & Huxley (1952*b*)

* Exact value chosen to make the total ionic current zero at the resting potential ($V=0$).

† The experimental values for $\bar{g}_{Na}$ were obtained by multiplying the peak sodium conductances by factors derived from the values chosen for α_m, β_m, α_h, and β_h.

Downloaded from jp.physoc.org by on January 29, 2008

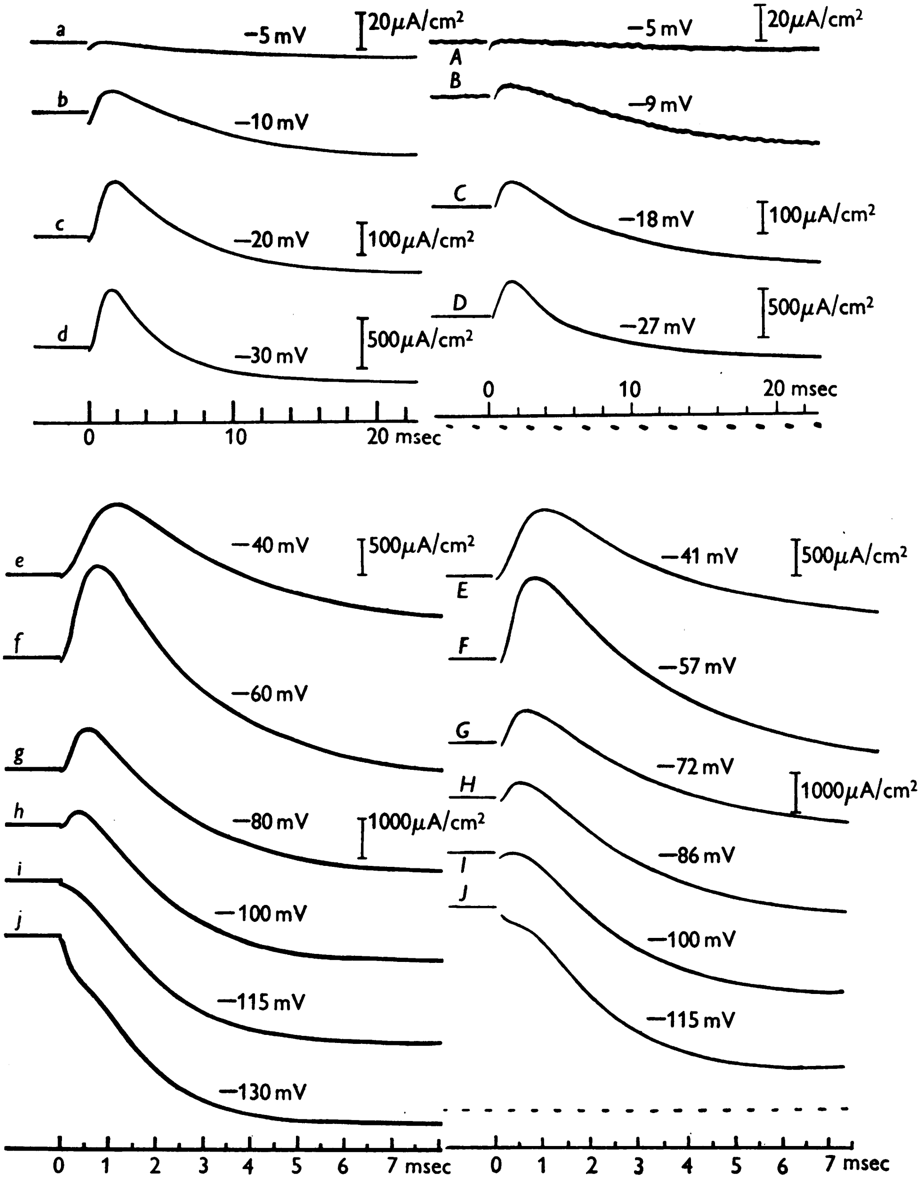

Fig. 11. Left-hand column: time course of membrane current during voltage clamp, calculated for temperature of 4° C from eqn. (26) and subsidiaries and plotted on the same scale as the experimental curves in the right-hand column. Right-hand column: observed time course of membrane currents during voltage clamp. Axon 31 at 4° C; compensated feedback. The time scale changes between *d*, *D* and *e*, *E*. The current scale changes after *b*, *B*; *c*, *C*; *d*, *D* and *f*, *F*.

Downloaded from jp.physoc.org by on January 29, 2008

considered. There is no current along the axis cylinder and the net membrane current must therefore always be zero, except during the stimulus. If the stimulus is a short shock at $t=0$, the form of the action potential should be given by solving eqn. (26) with $I=0$ and the initial conditions that $V=V_0$ and m, n and h have their resting steady state values, when $t=0$.

The situation is more complicated in a propagated action potential. The fact that the local circuit currents have to be provided by the net membrane current leads to the well-known relation

$$i=\frac{1}{r_1+r_2}\frac{\partial^2 V}{\partial x^2}, \tag{27}$$

where i is the membrane current per unit length, r_1 and r_2 are the external and internal resistances per unit length, and x is distance along the fibre. For an axon surrounded by a large volume of conducting fluid, r_1 is negligible compared with r_2. Hence

$$i=\frac{1}{r_2}\frac{\partial^2 V}{\partial x^2},$$

or

$$I=\frac{a}{2R_2}\frac{\partial^2 V}{\partial x^2}, \tag{28}$$

where I is the membrane current density, a is the radius of the fibre and R_2 is the specific resistance of the axoplasm. Inserting this relation in eqn. (26), we have

$$\frac{a}{2R_2}\frac{\partial^2 V}{\partial x^2}=C_M\frac{\partial V}{\partial t}+\bar{g}_K n^4 (V-V_K)+\bar{g}_{Na} m^3 h (V-V_{Na})+\bar{g}_l (V-V_l), \tag{29}$$

the subsidiary equations being unchanged.

Equation (29) is a partial differential equation, and it is not practicable to solve it as it stands. During steady propagation, however, the curve of V against time at any one position is similar in shape to that of V against distance at any one time, and it follows that

$$\frac{\partial^2 V}{\partial x^2}=\frac{1}{\theta^2}\frac{\partial^2 V}{\partial t^2},$$

where θ is the velocity of conduction. Hence

$$\frac{a}{2R_2\theta^2}\frac{\mathrm{d}^2 V}{\mathrm{d}t^2}=C_M\frac{\mathrm{d}V}{\mathrm{d}t}+\bar{g}_K n^4 (V-V_K)+\bar{g}_{Na} m^3 h (V-V_{Na})+\bar{g}_l (V-V_l). \tag{30}$$

This is an ordinary differential equation and can be solved numerically, but the procedure is still complicated by the fact that θ is not known in advance. It is necessary to guess a value of θ, insert it in eqn. (30) and carry out the numerical solution starting from the resting state at the foot of the action potential. It is then found that V goes off towards either $+\infty$ or $-\infty$, according as the guessed θ was too small or too large. A new value of θ is

Downloaded from jp.physoc.org by on January 29, 2008

then chosen and the procedure repeated, and so on. The correct value brings V back to zero (the resting condition) when the action potential is over.

The solutions which go towards $\pm\infty$ correspond to action potentials travelling slower than normal under a travelling anode or faster than normal under a travelling cathode. We suspect that a system which tends to $-\infty$ for all values of θ after an initial negative displacement of V is one which is incapable of propagating an action potential.

NUMERICAL METHODS

Membrane action potentials

Integration procedure. The equations to be solved are the four simultaneous first-order equations (26), (7), (15), and (16) (p. 518). After slight rearrangement (which will be omitted in this description) these were integrated by the method of Hartree (1932–3). Denoting the beginning and end of a step by t_0 and t_1 $(=t_0+\delta t)$ the procedure for each step was as follows:

(1) Estimate V_1 from V_0 and its backward differences.

(2) Estimate n_1 from n_0 and its backward differences.

(3) Calculate $(\mathrm{d}n/\mathrm{d}t)_1$ from eqn. 7 using the estimated n_1 and the values of α_n and β_n appropriate to the estimated V_1.

(4) Calculate n_1 from the equation

$$n_1-n_0=\frac{\delta t}{2}\left\{\left(\frac{\mathrm{d}n}{\mathrm{d}t}\right)_0+\left(\frac{\mathrm{d}n}{\mathrm{d}t}\right)_1-\frac{1}{12}\left[\Delta^2\left(\frac{\mathrm{d}n}{\mathrm{d}t}\right)_0+\Delta^2\left(\frac{\mathrm{d}n}{\mathrm{d}t}\right)_1\right]\right\};$$

$\Delta^2(\mathrm{d}n/\mathrm{d}t)$ is the second difference of $\mathrm{d}n/\mathrm{d}t$; its value at t_1 has to be estimated.

(5) If this value of n_1 differs from that estimated in (2), repeat (3) and (4) using the new n_1. If necessary, repeat again until successive values of n_1 are the same.

(6) Find m_1 and h_1 by procedures analogous to steps (2)–(5).

(7) Calculate $\bar{g}_{\mathrm{K}}n_1^4$ and $\bar{g}_{\mathrm{Na}}m_1^3h_1$.

(8) Calculate $(\mathrm{d}V/\mathrm{d}t)_1$ from eqn. 26 using the values found in (7) and the originally estimated V_1.

(9) Calculate a corrected V_1 by procedures analogous to steps (4) and (5). This result never differed enough from the original estimated value to necessitate repeating the whole procedure from step (3) onwards.

The step value had to be very small initially (since there are no differences at $t=0$) and it also had to be changed repeatedly during a run, because the differences became unmanageable if it was too large. It varied between about 0·01 msec at the beginning of a run or 0·02 msec during the rising phase of the action potential, and 1 msec during the small oscillations which follow the spike.

Accuracy. The last digit retained in V corresponded to microvolts. Sufficient digits were kept in the other variables for the resulting errors in the change of V at each step to be only occasionally as large as 1 μV. It is difficult to estimate the degree to which the errors at successive steps accumulate, but we are confident that the overall errors are not large enough to be detected in the illustrations of this paper.

Temperature differences. In calculating the action potential it was convenient to use tables giving the α's and β's at intervals of 1 mV. The tabulated values were appropriate to a fibre at 6·3° C. To obtain the action potential at some other temperature T' °C the direct method would be to multiply all α's and β's by a factor $\phi=3^{(T'-6\cdot3)/10}$, this being correct for a Q_{10} of 3. Inspection of eqn. 26 shows that the same result is achieved by calculating the action potential at 6·3° C with a membrane capacity of ϕC_M μF/cm^2, the unit of time being $1/\phi$ msec. This method was adopted since it saved recalculating the tables.

Downloaded from jp.physoc.org by on January 29, 2008

Propagated action potential

Equations. The main equation for a propagated action potential is eqn. (30). Introducing a quantity $K=2R_2\theta^2C_M/a$, this becomes

$$\frac{d^2V}{dt^2}=K\left\{\frac{dV}{dt}+\frac{1}{C_M}[\bar{g}_K n^4(V-V_K)+\bar{g}_{Na}m^3h(V-V_{Na})+\bar{g}_l(V-V_l)]\right\}. \tag{31}$$

The subsidiary equations (7), (15) and (16), and the α's and β's, are the same as for the membrane equation.

Integration procedure. Steps (1)–(7) were the same as for the membrane action potential. After that the procedure was as follows:

(8) Estimate $(dV/dt)_1$ from $(dV/dt)_0$ and its backward differences.

(9) Calculate $(d^2V/dt^2)_1$ from eqn. (31), using the values found in (7) and the estimated values of V_1 and $(dV/dt)_1$.

(10) Calculate a corrected $(dV/dt)_1$ by procedures analogous to steps (4) and (5).

(11) Calculate a corrected V_1 by a procedure analogous to step (4), using the corrected $(dV/dt)_1$.

(12) If necessary, repeat (9)–(11) using the new V_1 and $(dV/dt)_1$, until successive values of V_1 agree.

Starting conditions. In practice it is necessary to start with V deviating from zero by a finite amount (0·1 mV was used). The first few values of V, and hence the differences, were obtained as follows. Neglecting the changes in g_K and g_{Na}, eqn. (31) is

$$\frac{d^2V}{dt^2}=K\left\{\frac{dV}{dt}+\frac{g_0}{C_M}V\right\},$$

where g_0 is the resting conductance of the membrane. The solution of this equation is $V=V_0e^{\mu t}$, where μ is a solution of

$$\mu^2-K\mu-Kg_0/C_M=0. \tag{32}$$

When K has been chosen, μ can thus be found and hence V_1, V_2, etc. ($V_0e^{\mu t_1}$, $V_0e^{\mu t_2}$, etc.).

After several runs had been calculated, so that K was known within fairly narrow limits, time was saved by starting new runs not from near $V=0$ but from a set of values interpolated between corresponding points on a run which had gone towards $+\infty$ and another which had gone towards $-\infty$.

Choice of K. The value of K chosen for the first run makes no difference to the final result, but the nearer it is to the correct value the fewer runs will need to be evaluated. The starting value was found by inserting in eqn. (32) a value of μ found by measuring the foot of an observed action potential.

Calculation of falling phase. The procedure outlined above is satisfactory for the rising phase and peak of the action potential but becomes excessively tedious in the falling phase and the oscillations which follow the spike. A different method, which for other reasons is not applicable in the earlier phases, was therefore employed. The solution was continued as a membrane action potential, and the value of d^2V/dt^2 calculated at each step from the differences of dV/dt. From these it was possible to derive an estimate of the values (denoted by z) that d^2V/dt^2 would have taken in a propagated action potential. The membrane solution was then re-calculated using the following equation instead of eqn. (31):

$$\frac{dV}{dt}=-\frac{1}{C_M}\{\bar{g}_K n^4(V-V_K)+\bar{g}_{Na}m^3h(V-V_{Na})+\bar{g}_l(V-V_l)\}+\frac{z}{K}. \tag{33}$$

This was repeated until the z's assumed for a particular run agreed with the d^2V/dt^2's derived from the same run. When this is the case, eqn. (33) is identical with eqn. (31), the main equation for the propagated action potential.

Downloaded from jp.physoc.org by on January 29, 2008

RESULTS

Membrane action potentials

Form of action potential at 6° C. Three calculated membrane action potentials, with different strengths of stimulus, are shown in the upper part of Fig. 12. Only one, in which the initial displacement of membrane potential was 15 mV, is complete; in the other two the calculation was not carried beyond the middle of the falling phase because of the labour involved and because the solution had become almost identical with the 15 mV action potential, apart from the displacement in time. One solution for a stimulus just below threshold is also shown.

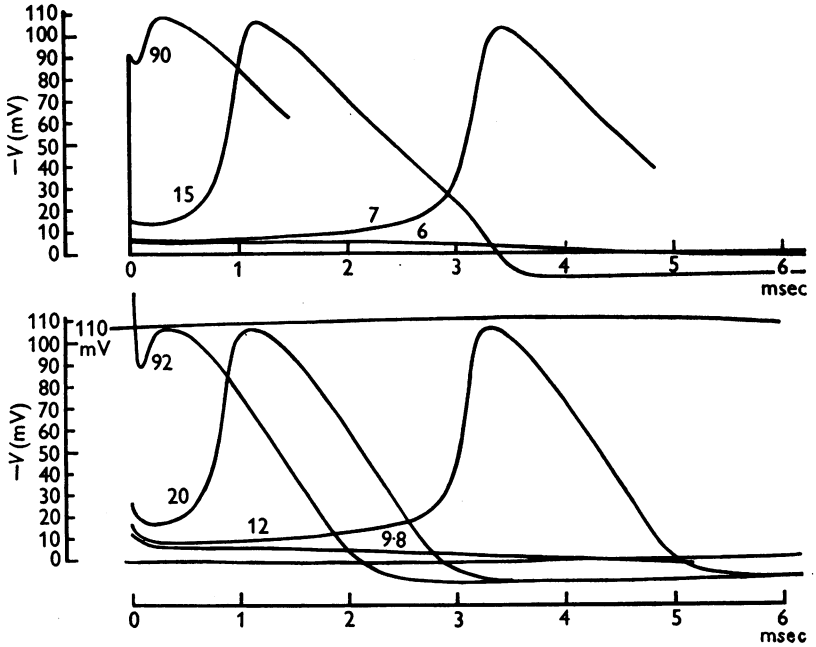

Fig. 12. Upper family: solutions of eqn. (26) for initial depolarizations of 90, 15, 7 and 6 mV (calculated for 6° C). Lower family: tracings of membrane action potentials recorded at 6° C from axon 17. The numbers attached to the curves give the shock strength in mμcoulomb/cm^2. The vertical and horizontal scales are the same in both families (apart from the slight curvature indicated by the 110 mV calibration line). In this and all subsequent figures depolarizations (or negative displacements of *V*) are plotted upwards.

The lower half of Fig. 12 shows a corresponding series of experimental membrane action potentials. It will be seen that the general agreement is good, as regards amplitude, form and time-scale. The calculated action potentials do, however, differ from the experimental in the following respects: (1) The drop during the first 0·1 msec is smaller. (2) The peaks are sharper.

Downloaded from jp.physoc.org by on January 29, 2008

(3) There is a small hump in the lower part of the falling phase. (4) The ending of the falling phase is too sharp. The extent to which these differences are the result of known shortcomings in our formulation will be discussed on pp. 542–3.

The positive phase of the calculated action potential has approximately the correct form and duration, as may be seen from Fig. 13 in which a pair of curves are plotted on a slower time scale.

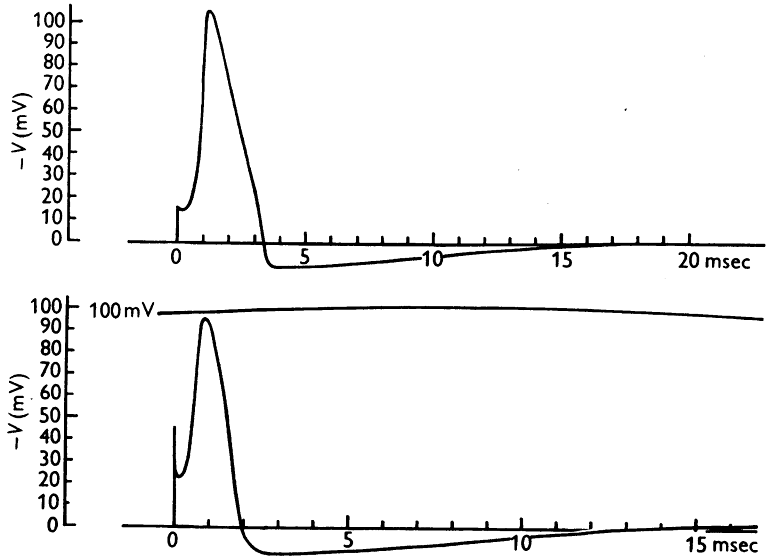

Fig. 13. Upper curve: solution of eqn. (26) for initial depolarization of 15 mV, calculated for 6° C. Lower curve: tracing of membrane action potential recorded at 9·1° C (axon 14). The vertical scales are the same in both curves (apart from curvature in the lower record). The horizontal scales differ by a factor appropriate to the temperature difference.

Certain measurements of these and other calculated action potentials are collected in Table 4.

Form of action potential at 18·5° C. Fig. 14 shows a comparison between a calculated membrane action potential at 18·5° C and an experimental one at 20·5° C. The same differences can be seen as at the low temperature, but, except for the initial drop, they are less marked. In both the calculated and the experimental case, the rise of temperature has greatly reduced the duration of the spike, the difference being more marked in the falling than in the rising phase (Table 4), as was shown in propagated action potentials by Hodgkin & Katz (1949).

The durations of both falling phase and positive phase are reduced at the higher temperature by factors which are not far short of that (3·84) by which the rate constants of the permeability changes are raised ($Q_{10} = 3{\cdot}0$). This is the justification for the differences in time scale between the upper and lower parts in Figs. 13 and 14.

Downloaded from jp.physoc.org by on January 29, 2008

TABLE 4. Characteristics of calculated action potentials

Type of action potential	Temperature (°C)	Stimulus	Spike height (mV)	Amplitude of positive phase (mV)	Peak conductance (m.mho/cm²)	Duration of rising phase, 20 mV to peak (msec)	Duration of falling phase, peak to $V=0$ (msec)	Duration of positive phase (msec)	Interval from peak of potential to peak of conductance (msec)	Max. rate of rise (V/sec)
Propagated	18·5	—	90·5	9·7	32·6	0·252	0·67	5·20	−0·016	431
Membrane	18·5	15 mV depolarization	96·8	10·5	30·7	0·275	0·61	5·09	+0·012	564
Membrane	6·3	100 mV depolarization	108·8	—	45·5	—	—	—	+0·16	—
Membrane	6·3	90 mV depolarization	108·5	—	44·8	—	—	—	+0·15	—
Membrane	6·3	15 mV depolarization	105·4	11·2	37·0	0·59	2·21	14·15	+0·15	311
Membrane	6·3	7 mV depolarization	102·1	—	33·4	0·62	—	—	+0·16	277
Membrane	6·3	Anode break	112·1	11·2	53·4	0·50	2·54	14·4	+0·14	414

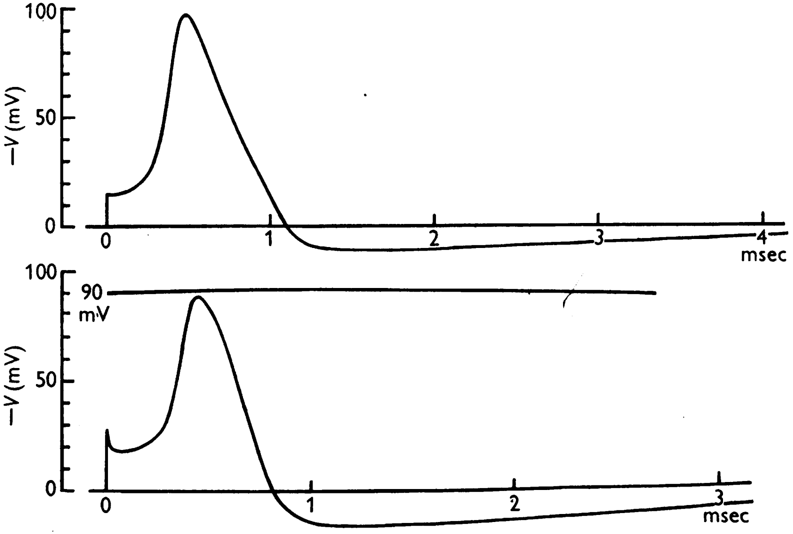

Fig. 14. Upper curve: solution of eqn. (26) for initial depolarization of 15 mV, calculated for 18·5° C. Lower curve: tracing of membrane action potential recorded at 20·5° C (axon 11). Vertical scales are similar. Horizontal scales differ by a factor appropriate to the temperature difference.

Downloaded from jp.physoc.org by on January 29, 2008

Propagated action potential

Form of propagated action potential. Fig. 15 compares the calculated propagated action potential, at 18·5° C, with experimental records on both fast and slow time bases. As in the case of the membrane action potential, the only differences are in certain details of the form of the spike.

Velocity of conduction. The value of the constant K that was found to be needed in the equation for the propagated action potential (eqn. 31) was 10·47 msec^{-1}. This constant, which depends only on properties of the membrane, determines the conduction velocity in conjunction with the constants of the nerve fibre considered as a cable. The relation is given by the definition of K (p. 524), from which

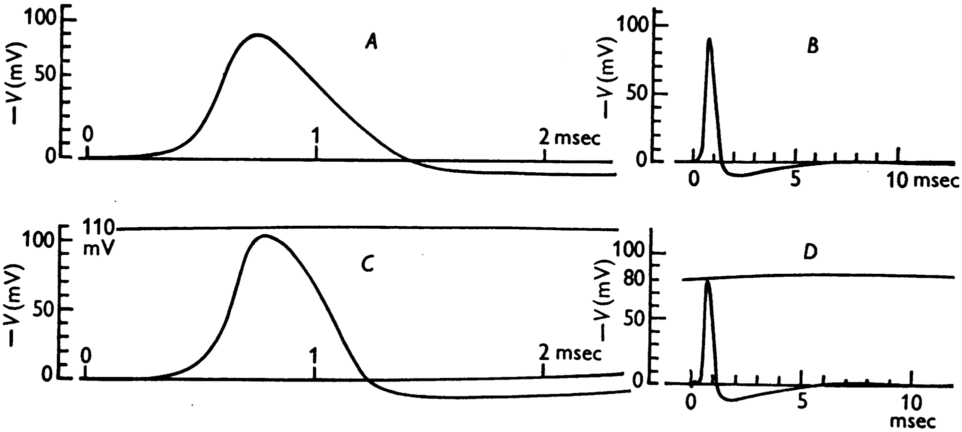

Fig. 15. *A*, solution of eqn. (31) calculated for K of 10·47 msec^{-1} and temperature of 18·5° C. *B*, same solution plotted on slower time scale. *C*, tracing of propagated action potential on same vertical and horizontal scales as *A*. Temperature 18·5° C. *D*, tracing of propagated action potential from another axon on approximately the same vertical and horizontal scales as *B*. Temperature 19·2° C. This axon had been used for several hours; its spike was initially 100 mV.

$$\theta = \sqrt{(Ka/2R_2C_M)}, \tag{34}$$

where θ = conduction velocity, a = radius of axis cylinder, R_2 = specific resistance of axoplasm, and C_M = capacity per unit area of membrane.

The propagated action potential was calculated for the temperature at which the record C of Fig. 15 was obtained, and with the value of C_M (1·0 μF/cm^2) that was measured on the fibre from which that record was made. Since θ, a and R_2 were also measured on that fibre, a direct comparison between calculated and observed velocities is possible. The values of a and R_2 were 238 μ and 35·4 Ω. cm respectively. Hence the calculated conduction velocity is

$$(10470 \times 0{\cdot}0238/2 \times 35{\cdot}4 \times 10^{-6})^{\frac{1}{2}} \text{ cm/sec} = 18{\cdot}8 \text{ m/sec.}$$

The velocity found experimentally in this fibre was 21·2 m/sec.

Downloaded from jp.physoc.org by on January 29, 2008

Impedance changes

Time course of conductance change. Cole & Curtis (1939) showed that the impedance of the membrane fell during a spike, and that the fall was due to a great increase in the conductance which is in parallel with the membrane capacity. An effect of this kind is to be expected on our formulation, since the entry of Na^+ which causes the rising phase, and the loss of K^+ which causes the falling phase, are consequent on increases in the conductance of the membrane to currents carried by these ions. These component conductances are evaluated during the calculation, and the total conductance is obtained by adding them and the constant 'leak conductance', $\bar{g}_l$.

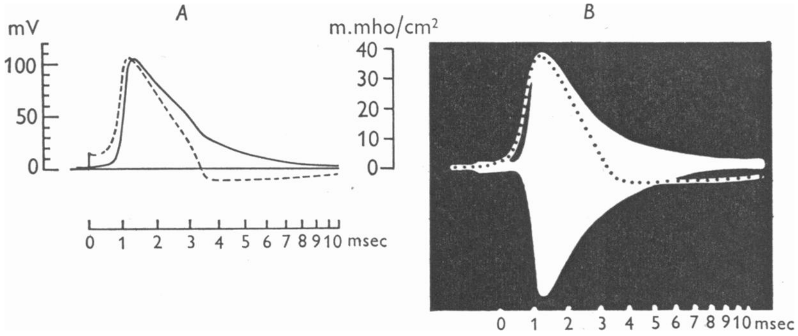

Fig. 16. *A*, solution of eqn. (26) for initial depolarization of 15 mV at a temperature of 6° C. The broken curve shows the membrane action potential in mV; the continuous curve shows the total membrane conductance ($g_{\mathrm{Na}}+g_{\mathrm{K}}+\bar{g}_l$) as a function of time. *B*, records of propagated action potential (dotted curve) and conductance change reproduced from Cole & Curtis (1939). The time scales are the same in *A* and *B*.

Fig. 16*A* shows the membrane potential and conductance in a calculated membrane action potential. For comparison, Fig. 16*B* shows superposed records of potential and impedance bridge output (proportional to conductance change), taken from Cole & Curtis's paper. The time scale is the same in *B* as in *A*, and the curves have been drawn with the same peak height. It will be seen that the main features of Cole & Curtis's record are reproduced in the calculated curve. Thus (1) the main rise in conductance begins later than the rise of potential; (2) the conductance does not fall to its resting value until late in the positive phase; and (3) the peak of the conductance change occurs at nearly the same time as the peak of potential. The exact time relation between the peaks depends on the conditions, as can be seen from Table 4.

We chose a membrane action potential for the comparison in Fig. 16 because the spike duration shows that the experimental records were obtained at about 6° C, and our propagated action potential was calculated for 18·5° C. The conductance during the latter is plotted together with the potential in Fig. 17. The same features are seen as in the membrane action potential, the delay

Downloaded from jp.physoc.org by on January 29, 2008

between the rise of potential and the rise of conductance being even more marked.

Absolute value of peak conductance. The agreement between the height of the conductance peak in Fig. 16*A* and the half-amplitude of the bridge output in Fig. 16*B* is due simply to the choice of scale. Nevertheless, our calculated action potentials agree well with Cole & Curtis's results in this respect. These authors found that the average membrane resistance at the peak of the impedance change was 25 Ω.cm², corresponding to a conductance of 40 m.mho/cm². The peak conductances in our calculated action potentials ranged from 31 to 53 m.mho/cm² according to the conditions, as shown in Table 4.

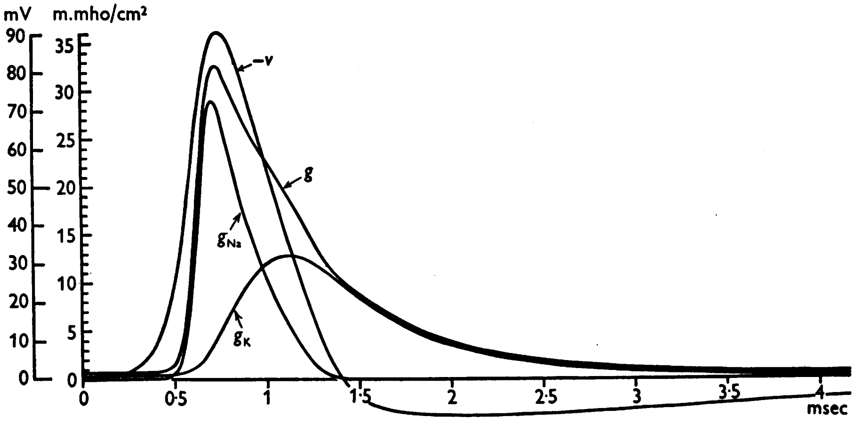

Fig. 17. Numerical solution of eqn. (31) showing components of membrane conductance (g) during propagated action potential ($-V$). Details of the analysis are as in Fig. 15.

Components of conductance change. The manner in which the conductances to Na^+ and K^+ contribute to the change in total conductance is shown in Fig. 17 for the calculated propagated action potential. The rapid rise is due almost entirely to sodium conductance, but after the peak the potassium conductance takes a progressively larger share until, by the beginning of the positive phase, the sodium conductance has become negligible. The tail of raised conductance that falls away gradually during the positive phase is due solely to potassium conductance, the small constant leak conductance being of course present throughout.

Ionic movements

Time course of ionic currents. The time course of the components of membrane current carried by sodium and potassium ions during the calculated propagated spike is shown in Fig. 18 *C*. The total ionic current contains also a small contribution from 'leak current' which is not plotted separately.

Two courses are open to current which is carried into the axis cylinder by ions crossing the membrane: it may leave the axis cylinder again by altering

Downloaded from jp.physoc.org by on January 29, 2008

the charge on the membrane capacity, or it may turn either way along the axis cylinder making a net contribution, I, to the local circuit current. The magnitudes of these two terms during steady propagation are $-C_M \mathrm{d}V/\mathrm{d}t$ and $(C_M/K)\,\mathrm{d}^2V/\mathrm{d}t^2$ respectively, and the manner in which the ionic current is divided between them at the different stages of the spike is shown in Fig. 18*B*. It will be seen that the ionic current is very small until the potential is well beyond the threshold level, which is shown by Fig. 12*A* to be about 6 mV.

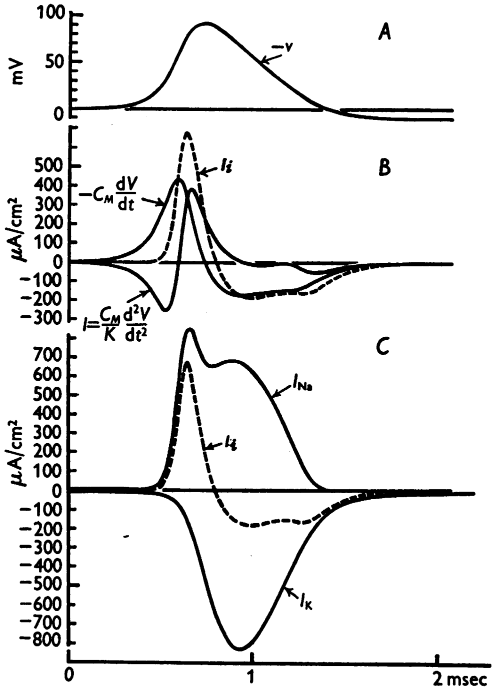

Fig. 18. Numerical solution of eqn. (31) showing components of membrane current during propagated action potential. *A*, membrane potential ($-V$). *B*, ionic current (I_i), capacity current $\left(-C_M\frac{\mathrm{d}V}{\mathrm{d}t}\right)$ and total membrane current $\left(I=\frac{C_M}{K}\frac{\mathrm{d}^2V}{\mathrm{d}t^2}\right)$. *C*, ionic current ($I_i$), sodium current ($I_{\mathrm{Na}}$) and potassium current (I_{K}). The time scale applies to all the curves. Details of the analysis are as in Fig. 15.

During this period the current for charging the membrane capacity comes almost entirely from local circuits. The fact that the ionic current does not become appreciable as soon as the threshold depolarization is passed is due partly to the smallness of the currents reached in any circumstances near the threshold, and partly to the delay with which sodium conductance rises when the potential is lowered.

Total movements of ions. The total entry of sodium and loss of potassium can be obtained by integrating the corresponding ionic currents over the whole

Downloaded from jp.physoc.org by on January 29, 2008

impulse. This has been done for the four complete action potentials that we calculated, and the results are given in Table 5. It will be seen that the results at 18·5° C are in good agreement with the values found experimentally by Keynes (1951) and Keynes & Lewis (1951), which were obtained at comparable temperatures.

Ionic fluxes. The flux in either direction of an ion can be obtained from the net current and the equilibrium potential for that ion, if the independence principle (Hodgkin & Huxley, 1952*a*) is assumed to hold. Thus the outward flux of sodium ions is $I_{\mathrm{Na}}/(\exp{(V-V_{\mathrm{Na}})\,F/RT}-1)$, and the inward flux of potassium ions is $-I_{\mathrm{K}}/(\exp{(V_{\mathrm{K}}-V)\,F/RT}-1)$. These two quantities were evaluated at each step of the calculated action potentials, and integrated over the whole impulse. The integrated flux in the opposite direction is given in each case by adding the total net movement. The results are given in Table 5, where they can be compared with the results obtained with radioactive tracers by Keynes (1951) on *Sepia* axons. It will be seen that our theory predicts too little exchange of Na and too much exchange of K during an impulse. This discrepancy will be discussed later.

Refractory period

Time course of inactivation and delayed rectification. According to our theory, there are two changes resulting from the depolarization during a spike which make the membrane unable to respond to another stimulus until a certain time has elapsed. These are 'inactivation', which reduces the level to which the sodium conductance can be raised by a depolarization, and the delayed rise in potassium conductance, which tends to hold the membrane potential near to the equilibrium value for potassium ions. These two effects are shown in Fig. 19 for the calculated membrane action potential at 6° C. Both curves reach their normal levels again near the end of the positive phase, and finally

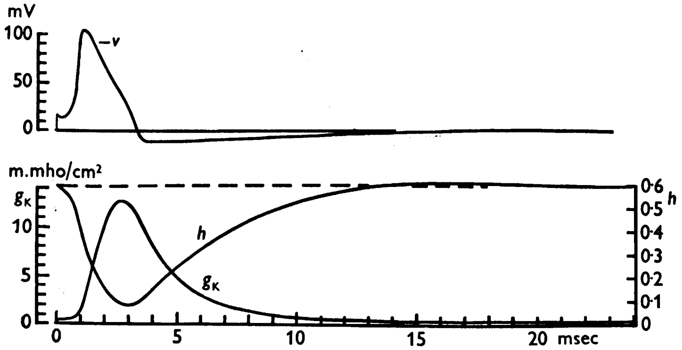

Fig. 19. Numerical solution of eqn. (26) for initial depolarization of 15 mV and temperature of 6° C. Upper curve: membrane potential, as in Fig. 13. Lower curves show time course of g_{K} and h during action potential and refractory period.

Downloaded from jp.physoc.org by on January 29, 2008

TABLE 5. Ionic movements during an impulse. All values are expressed in $\mu\mu$mole/cm^2 and represent the excess over the corresponding movement in the resting state. In the theoretical cases the integration is taken as far as the 3rd intersection with the base line after the spike; it is begun in case (1) when $V = 0{\cdot}1$ mV; (2) and (3) at the stimulus; (4) when $V = 0$ before the spike. Experimental data from Keynes (1951) for row 6 and from Keynes & Lewis (1951) for rows 5 and 7.

	Type of action potential	Temp. (° C)	Stimulus (mV)	Sodium			Potassium		
				Influx	Outflux	Net entry	Influx	Outflux	Net loss
Theoretical (*Loligo*):									
1	Propagated	18·5	—	5·42	1·09	4·33	1·72	5·98	4·26
2	Membrane	18·5	15	5·01	1·02	3·99	1·71	5·78	4·07
3	Membrane	6·3	15	19·30	4·84	14·46	6·17	20·49	14·32
4	Membrane	6·3	Anode break	26·61	9·45	17·16	6·64	23·41	16·77
Experimental:									
5	Propagated (*Loligo*)	22	—	—	—	3·5	—	—	3·0
6	Propagated (*Sepia*)	14	—	10·3	6·6	3·7	0·39	4·7	4·3
7	Propagated (*Sepia*)	22	—	—	—	3·8	—	—	3·6

Downloaded from jp.physoc.org by on January 29, 2008

settle down after a heavily damped oscillation of small amplitude which is not seen in the figure.

Responses to stimuli during positive phase. We calculated the responses of the membrane when it was suddenly depolarized by 90 mV at various times during the positive phase of the membrane action potential at 6° C. These are shown by the upper curves in Fig. 20. After the earliest stimulus the membrane potential falls again with hardly a sign of activity, and the membrane can be said to be in the 'absolute refractory period'. The later stimuli produce action potentials of increasing amplitude, but still smaller than the control; these are in the 'relative refractory period'. Corresponding experimental curves are shown in the lower part of Fig. 20. The agreement is good, as regards both the duration of the absolute refractory period and the changes in shape of the spike as recovery progresses.

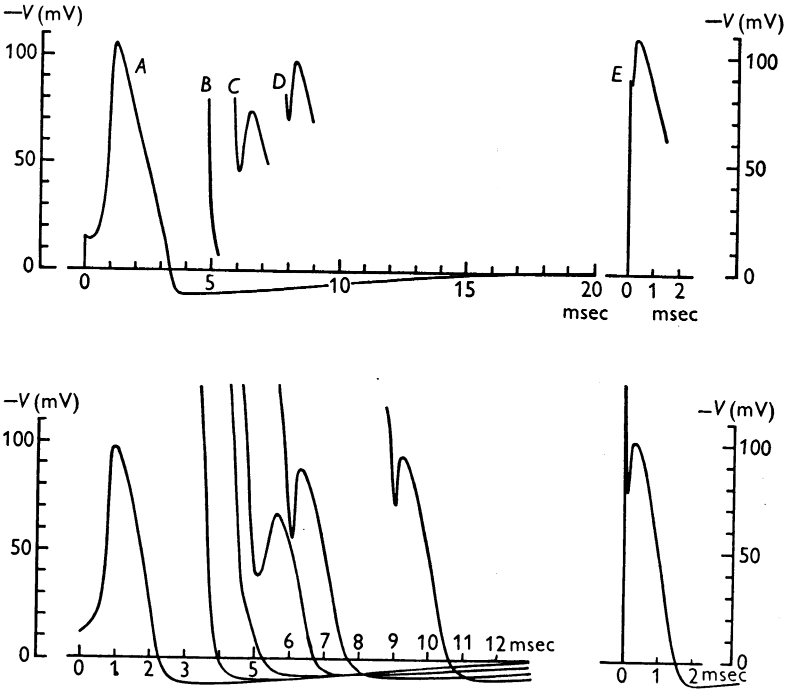

Fig. 20. Theoretical basis of refractory period. Upper curves: numerical solutions of eqn. (26) for temperature of 6° C. Curve A gives the response to 15 mμcoulomb/cm^2 applied instantaneously at $t=0$. Curve E gives the response to 90 mμcoulomb/cm^2 again applied in the resting state. Curves B to D show effect of applying 90 mμcoulomb/cm^2 at various times after curve A. Lower curves: a similar experiment with an actual nerve, temperature 9° C. The voltage scales are the same throughout. The time scales differ by a factor appropriate to the temperature difference.

Downloaded from jp.physoc.org by on January 29, 2008

Excitation

Our calculations of excitation processes were all made for the case where the membrane potential is uniform over the whole area considered, and not for the case of local stimulation of a whole nerve. There were two reasons for this: first, that such data from the squid giant fibre as we had for comparison were obtained by uniform stimulation of the membrane with the long electrode; and, secondly, that calculations for the whole nerve case would have been extremely laborious since the main equation is then a partial differential equation.

Threshold. The curves in Figs. 12 and 21 show that the theoretical 'membrane' has a definite threshold when stimulated by a sudden displacement of membrane potential. Since the initial fall after the stimulus is much less marked in these than in the experimental curves, it is relevant to compare the lowest point reached in a just threshold curve, rather than the magnitude of the original displacement. In the calculated series this is about 6 mV and in the experimental about 8 mV. This agreement is satisfactory, especially as the value for the calculated series must depend critically on such things as the leak conductance, whose value was not very well determined experimentally.

The agreement might have been somewhat less good if the comparison had been made at a higher temperature. The calculated value would have been much the same, but the experimental value in the series at 23° C shown in Fig. 8 of Hodgkin *et al.* (1952) is about 15 mV. However, this fibre had been stored for 5 hr before use and was therefore not in exactly the same state as those on which our measurements were based.

Subthreshold responses. When the displacement of membrane potential was less than the threshold for setting up a spike, characteristic subthreshold responses were seen. One such response is shown in Fig. 12, while several are plotted on a larger scale in Fig. 21*B*. Fig. 21*A* shows for comparison the corresponding calculated responses of our model. The only appreciable differences, in the size of the initial fall and in the threshold level, have been mentioned already in other connexions.

During the positive phase which follows each calculated subthreshold response, the potassium conductance is raised and there is a higher degree of 'inactivation' than in the resting state. The threshold must therefore be raised in the same way as it is during the relative refractory period following a spike. This agrees with the experimental findings of Pumphrey, Schmitt & Young (1940).

Anode break excitation. Our axons with the long electrode in place often gave anode break responses at the end of a period during which current was made to flow inward through the membrane. The corresponding response of out theoretical model was calculated for the case in which a current sufficient

Downloaded from jp.physoc.org by on January 29, 2008

to bring the membrane potential to 30 mV above the resting potential was suddenly stopped after passing for a time long compared with all the time-constants of the membrane. To do this, eqn. (26) was solved with $I=0$ and the initial conditions that $V=+30$ mV, and m, n and h have their steady state values for $V=+30$ mV, when $t=0$. The calculation was made for a temperature

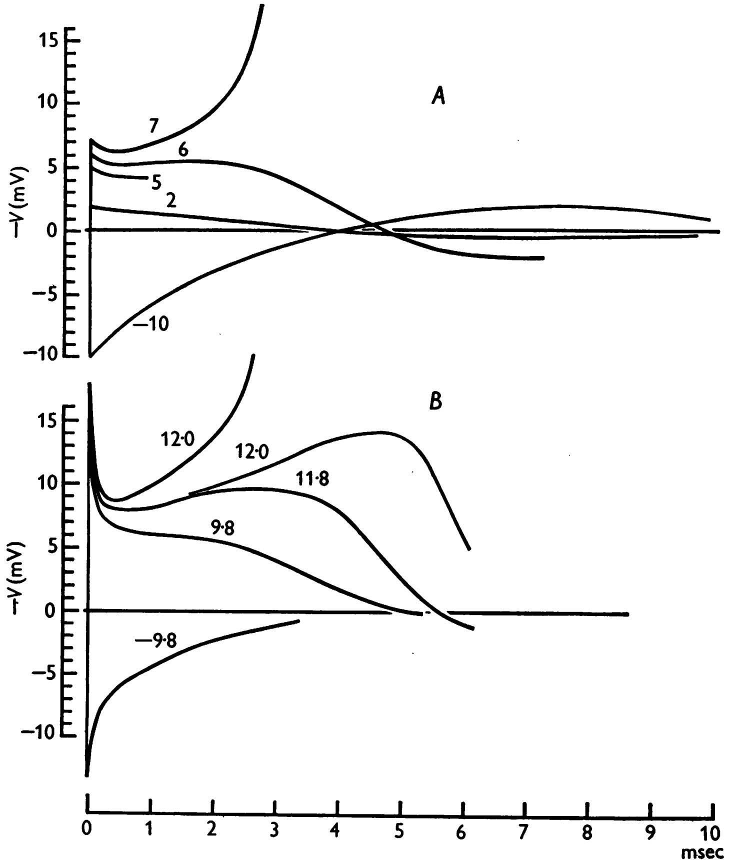

Fig. 21. *A*, numerical solutions of eqn. (26) for 6° C. The numbers attached to the curves give the initial depolarization in mV (also the quantity of charge applied in mμcoulomb/cm^2). *B*, response of nerve membrane at 6° C to short shocks; the numbers show the charge applied in mμcoulomb/cm^2. The curves have been replotted from records taken at low amplification and a relatively high time-base speed.

of 6·3° C. A spike resulted, and the time course of membrane potential is plotted in Fig. 22*A*. A tracing of an experimental anode break response is shown in Fig. 22*B*; the temperature is 18·5° C, no record near 6° being available. It will be seen that there is good general agreement. (The oscillations after the positive phase in Fig. 22*B* are exceptionally large; the response of

Downloaded from jp.physoc.org by on January 29, 2008

this axon to a small constant current was also unusually oscillatory as shown in Fig. 23.)

The basis of the anode break excitation is that anodal polarization decreases the potassium conductance and removes inactivation. These effects persist for an appreciable time so that the membrane potential reaches its resting value with a reduced outward potassium current and an increased inward sodium current. The total ionic current is therefore inward at $V=0$ and the membrane undergoes a depolarization which rapidly becomes regenerative.

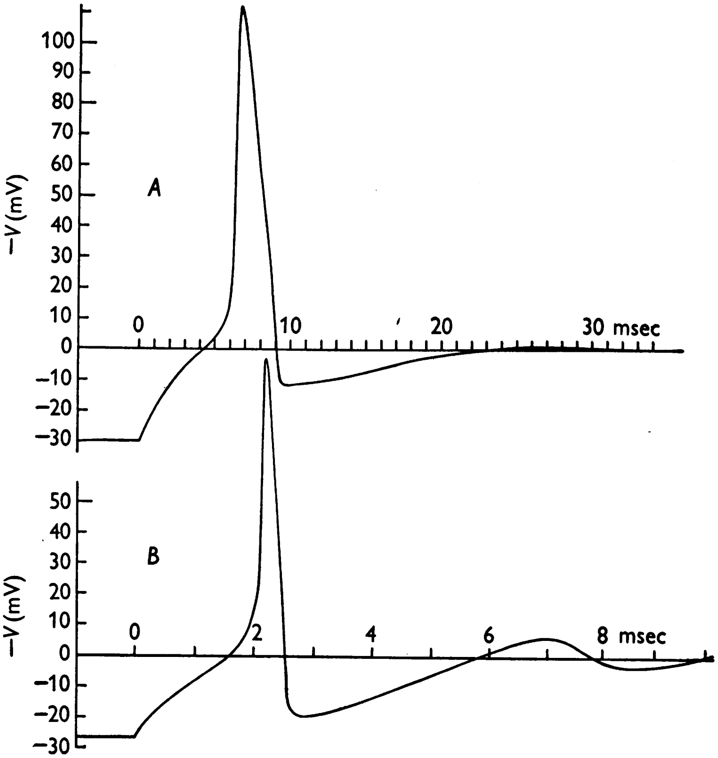

Fig. 22. Theoretical basis of anode break excitation. *A*, numerical solution of eqn. (26) for boundary condition $-V=-30$ mV for $t<0$; temperature 6° C. *B*, anode break excitation following sudden cessation of external current which had raised the membrane potential by 26·5 mV; giant axon with long electrode at 18·5° C. Time scales differ by a factor appropriate to the temperature difference.

Accommodation. No measurements of accommodation were made nor did we make any corresponding calculations for our model. It is clear, however, that the model will show 'accommodation' in appropriate cases. This may be shown in two ways. First, during the passage of a constant cathodal current through the membrane, the potassium conductance and the degree of inactivation will rise, both factors raising the threshold. Secondly, the steady state

Downloaded from jp.physoc.org by on January 29, 2008

ionic current at all strengths of depolarization is outward (Fig. 11), so that an applied cathodal current which rises sufficiently slowly will never evoke a regenerative response from the membrane, and excitation will not occur.

Oscillations

In all the calculated action potentials and subthreshold responses the membrane potential finally returns to its resting value with a heavily damped oscillation. This is well seen after subthreshold stimuli in Figs. 21*A* and 24, but the action potentials are not plotted on a slow enough time base or with a large enough vertical scale to show the oscillations which follow the positive phase.

The corresponding oscillatory behaviour of the real nerve could be seen after a spike or a subthreshold short shock, but was best studied by passing a small constant current through the membrane and recording the changes of membrane potential that resulted. The current was supplied by the long internal electrode so that the whole area of membrane was subjected to a uniform current density. It was found that when the current was very weak the potential changes resulting from inward current (anodal) were almost exactly similar to those resulting from an equal outward current, but with opposite sign. This is shown in Fig. 23*B* and *C*, where the potential changes are about ±1 mV. This symmetry with weak currents is to be expected from our equations, since they can be reduced to a linear form when the displacements of all the variables from their resting values are small. Thus, neglecting products, squares and higher powers of δV, δm, δn and δh, the deviations of V, m, n and h from their resting values (0, m_0, n_0 and h_0 respectively), eqn. (26) (p. 518) becomes

$$\delta I = C_M \frac{\mathrm{d}\delta V}{\mathrm{d}t} + \bar{g}_{\mathrm{K}} n_0^4 \delta V - 4\bar{g}_{\mathrm{K}} n_0^3 V_{\mathrm{K}} \delta n + \bar{g}_{\mathrm{Na}} m_0^3 h_0 \delta V$$
$$- 3\bar{g}_{\mathrm{Na}} m_0^2 h_0 V_{\mathrm{Na}} \delta m - \bar{g}_{\mathrm{Na}} m_0^3 V_{\mathrm{Na}} \delta h + \bar{g}_l \delta V. \qquad (35)$$

Similarly, eqn. (7) (p. 518) becomes

$$\frac{\mathrm{d}\delta n}{\mathrm{d}t} = \frac{\partial \alpha_n}{\partial V} \delta V - (\alpha_n + \beta_n)\, \delta n - n_0 \frac{\partial(\alpha_n + \beta_n)}{\partial V} \delta V,$$

or

$$(p + \alpha_n + \beta_n)\, \delta n = \left\{ \frac{\partial \alpha_n}{\partial V} - n_0 \frac{\partial(\alpha_n + \beta_n)}{\partial V} \right\} \delta V, \qquad (36)$$

where p represents d/dt, the operation of differentiating with respect to time.

The quantity δn can be eliminated between eqns. (35) and (36). This process is repeated for δm and δh, yielding a fourth-order linear differential equation with constant coefficients for δV. This can be solved by standard methods for any particular time course of the applied current density δI.

Downloaded from jp.physoc.org by on January 29, 2008

Fig. 23*A* shows the response of the membrane to a constant current pulse calculated in this way. The constants in the equations are chosen to be appropriate to a temperature of 18·5° C so as to make the result comparable with the tracings of experimental records shown in *B* and *C*. It will be seen that the calculated curve agrees well with the records in *B*, while those in *C*, obtained from another axon, are much less heavily damped and show a higher frequency of oscillation. A fair degree of variability is to be expected in these respects since both frequency and damping depend on the values of the components of the resting conductance. Of these, g_{Na} and g_{K} depend critically on the resting potential, while $\bar{g}_l$ is very variable from one fibre to another.

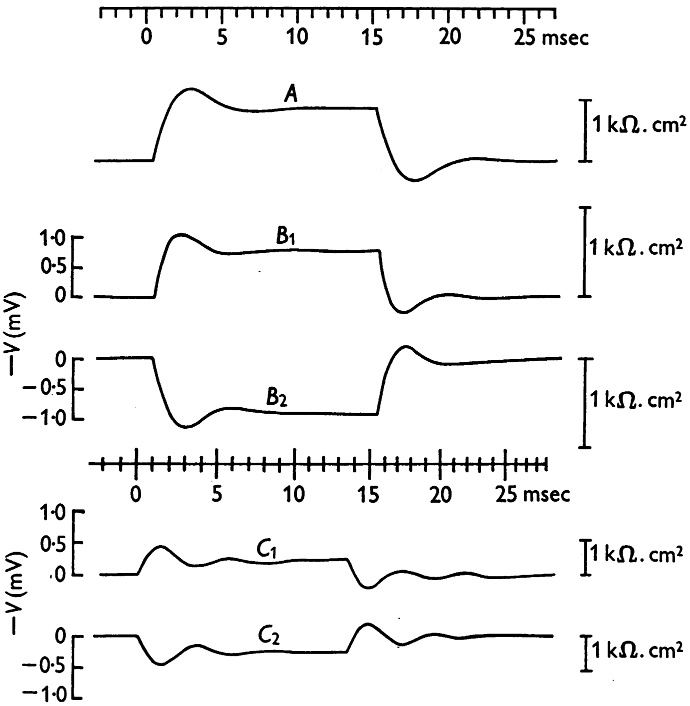

Fig. 23. *A*, solution of eqn. (35) for small constant current pulse; temperature 18·5° C; linear approximation. The curve shows $\delta V/\delta I$ (plotted upwards) as a function of time. *B*, changes in membrane potential associated with application of weak constant currents of duration 15 msec and strength $\pm 1{\cdot}49\,\mu\mathrm{A/cm}^2$. B_1, cathodic current; B_2, anodic current. Depolarization is shown upward. Temperature 19° C. *C*, similar records from another fibre enlarged to have same time scale. Current strengths are $\pm 0{\cdot}55\,\mu\mathrm{A/cm}^2$. Temperature 18° C. The response is unusually oscillatory.

Both theory and experiment indicate a greater degree of oscillatory behaviour than is usually seen in a cephalopod nerve in a medium of normal ionic composition. We believe that this is largely a direct result of using the long internal

Downloaded from jp.physoc.org by on January 29, 2008

electrode. If current is applied to a whole nerve through a point electrode, neighbouring points on the membrane will have different membrane potentials and the resulting currents in the axis cylinder will increase the damping.

The linear solution for the behaviour of the theoretical membrane at small displacements provided a convenient check on our step-by-step numerical procedure. The response of the membrane at 6·3° C to a small short shock was calculated by this means and compared with the step-by-step solution for an initial depolarization of the membrane by 2 mV. The results are plotted in Fig. 24. The agreement is very close, the step-by-step solution deviating in the direction that would be expected to result from its finite amplitude (cf. Fig. 21).

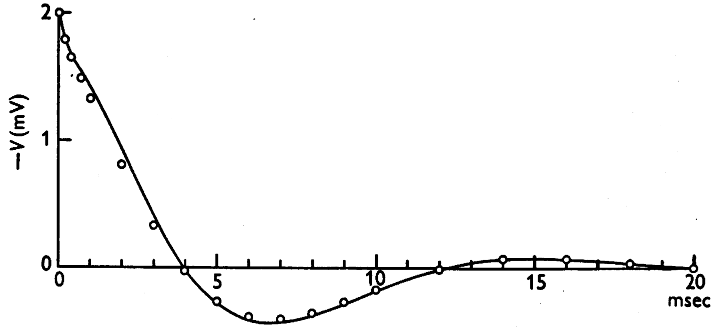

Fig. 24. Comparison of step-by-step solution and linear approximation. Eqn. (26), temperature 6° C; initial displacement of $-V = 2$ mV. Continuous line: step-by-step solution. Circles: linear approximation with same initial displacement.

As pointed out by Cole (1941), the process underlying oscillations in membrane potential must be closely connected with the inductive reactance observed with alternating currents. In our theoretical model the inductance is due partly to the inactivation process and partly to the change in potassium conductance, the latter being somewhat more important. For small displacements of the resting potential the variations in potassium current in 1 cm² of membrane are identical with those in a circuit containing a resistance of 820 Ω in series with an inductance which is shunted by a resistance of 1900 Ω. The value of the inductance is 0·39 H at 25° C, which is of the same order as the 0·2 H found by Cole & Baker (1941). The calculated inductance increases 3-fold for a 10° C fall in temperature and decreases rapidly as the membrane potential is increased; it disappears at the potassium potential and is replaced by a capacity for $E > E_K$.

DISCUSSION

The results presented here show that the equations derived in Part II of this paper predict with fair accuracy many of the electrical properties of the squid giant axon: the form, duration and amplitude of spike, both 'membrane'

Downloaded from jp.physoc.org by on January 29, 2008

and propagated; the conduction velocity; the impedance changes during the spike; the refractory period; ionic exchanges; subthreshold responses; and oscillations. In addition, they account at least qualitatively for many of the phenomena of excitation, including anode break excitation and accommodation. This is a satisfactory degree of agreement, since the equations and constants were derived entirely from 'voltage clamp' records, without any adjustment to make them fit the phenomena to which they were subsequently applied. Indeed any such adjustment would be extremely difficult, because in most cases it is impossible to tell in advance what effect a given change in one of the equations will have on the final solution.

The agreement must not be taken as evidence that our equations are anything more than an empirical description of the time-course of the changes in permeability to sodium and potassium. An equally satisfactory description of the voltage clamp data could no doubt have been achieved with equations of very different form, which would probably have been equally successful in predicting the electrical behaviour of the membrane. It was pointed out in Part II of this paper that certain features of our equations were capable of a physical interpretation, but the success of the equations is no evidence in favour of the mechanism of permeability change that we tentatively had in mind when formulating them.

The point that we do consider to be established is that fairly simple permeability changes in response to alterations in membrane potential, of the kind deduced from the voltage clamp results, are a sufficient explanation of the wide range of phenomena that have been fitted by solutions of the equations.

Range of applicability of the equations

The range of phenomena to which our equations are relevant is limited in two respects: in the first place, they cover only the short-term responses of the membrane, and in the second, they apply in their present form only to the isolated squid giant axon.

Slow changes. A nerve fibre whose membrane was described by our equations would run down gradually, since even in the resting state potassium leaves and sodium enters the axis cylinder, and both processes are accelerated by activity. This is no defect in describing the isolated squid giant axon, which does in fact run down in this way, but some additional process must take place in a nerve in the living animal to maintain the ionic gradients which are the immediate source of the energy used in impulse conduction.

After-potentials. Our equations give no account of after-potentials, apart from the positive phase and subsequent oscillations.

Conditions of isolated giant axon. There are many reasons for supposing that the resting potential of the squid giant axon is considerably lower after isolation than when it is intact in the living animal. Further evidence for this view

Downloaded from jp.physoc.org by on January 29, 2008

is provided by the observation (Hodgkin & Huxley, 1952*c*) that the maximum inward current that the membrane can pass on depolarization is increased by previously raising the resting potential by 10–20 mV by means of anodally directed current. Our equations could easily be modified to increase the resting potential (e.g. by reducing the leak conductance and adding a small outward current representing metabolic extrusion of sodium ions). We have not made any calculations for such a case, but certain qualitative results are evident from inspection of other solutions. If, for instance, the resting potential were raised (by 12 mV) to the potassium potential, the positive phase and subsequent oscillations after the spike would disappear, the rate of rise of the spike would be increased, the exchange of internal and external sodium in a spike would be increased, the membrane would not be oscillatory unless depolarized, and accommodation and the tendency to give anode break responses would be greatly reduced. Several of these phenomena have been observed when the resting potential of frog nerve is raised (Lorente de Nó, 1947), but no corresponding information exists about the squid giant axon.

Applicability to other tissues. The similarity of the effects of changing the concentrations of sodium and potassium on the resting and action potentials of many excitable tissues (Hodgkin, 1951) suggests that the basic mechanism of conduction may be the same as implied by our equations, but the great differences in the shape of action potentials show that even if equations of the same form as ours are applicable in other cases, some at least of the parameters must have very different values.

Differences between calculated and observed behaviour

In the Results section, a number of points were noted on which the calculated behaviour of our model did not agree with the experimental results. We shall now discuss the extent to which these discrepancies can be attributed to known shortcomings in our equations. Two such shortcomings were pointed out in Part II of this paper, and were accepted for the sake of keeping the equations simple. One was that the membrane capacity was assumed to behave as a 'perfect' condenser (phase angle 90°; p. 505), and the other was that the equations governing the potassium conductance do not give as much delay in the conductance rise on depolarization (e.g. to the sodium potential) as was observed in voltage clamps (p. 509).

The assumption of a perfect capacity probably accounts for the fact that the initial fall in potential after application of a short shock is much less marked in the calculated than in the experimental curves (Figs. 12 and 21). Some of the initial drop in the experimental curves may also be due to end-effects, the guard system being designed for the voltage clamp procedure but not for stimulation by short shocks.

Downloaded from jp.physoc.org by on January 29, 2008

The inadequacy of the delay in the rise of potassium conductance has several effects. In the first place the falling phase of the spike develops too early, reducing the spike amplitude slightly and making the peak too pointed in shape (p. 525). In the membrane action potentials these effects become more marked the smaller the stimulus, since the potassium conductance begins to rise during the latent period. This causes the spike amplitude to decrease more in the calculated than in the experimental curves (Fig. 12).

The low calculated value for the exchange of internal and external sodium ions is probably due to this cause. Most of the sodium exchange occurs near the peak of the spike, when the potential is close to the sodium potential. The early rise of potassium conductance prevents the potential from getting as close to the sodium potential, and from staying there for as long a time, as it should.

A check on these points is provided by the 'anode break' action potential. Until the break of the applied current, the quantity n has the steady state value appropriate to $V=+30$ mV, i.e. it is much smaller than in the usual resting condition. This greatly increases the delay in the rise of potassium conductance when the membrane is depolarized. It was found that the spike height was greater (Table 4), the peak was more rounded, and the exchange of internal and external sodium was greater (Table 5), than in an action potential which followed a cathodal short shock.

The other important respect in which the model results disagreed with the experimental was that the calculated exchange of internal and external potassium ions per impulse was too large. This exchange took place largely during the positive phase, when the potential is close to the potassium potential and the potassium conductance is still fairly high. We have no satisfactory explanation for this discrepancy, but it is probably connected with the fact that the value of the potassium potential was less strongly affected by changes in external potassium concentration than is required by the Nernst equation.

SUMMARY

1. The voltage clamp data obtained previously are used to find equations which describe the changes in sodium and potassium conductance associated with an alteration of membrane potential. The parameters in these equations were determined by fitting solutions to the experimental curves relating sodium or potassium conductance to time at various membrane potentials.

2. The equations, given on pp. 518–19, were used to predict the quantitative behaviour of a model nerve under a variety of conditions which corresponded to those in actual experiments. Good agreement was obtained in the following cases:

(*a*) The form, amplitude and threshold of an action potential under zero membrane current at two temperatures.

(*b*) The form, amplitude and velocity of a propagated action potential.

Downloaded from jp.physoc.org by on January 29, 2008

(*c*) The form and amplitude of the impedance changes associated with an action potential.

(*d*) The total inward movement of sodium ions and the total outward movement of potassium ions associated with an impulse.

(*e*) The threshold and response during the refractory period.

(*f*) The existence and form of subthreshold responses.

(*g*) The existence and form of an anode break response.

(*h*) The properties of the subthreshold oscillations seen in cephalopod axons.

3. The theory also predicts that a direct current will not excite if it rises sufficiently slowly.

4. Of the minor defects the only one for which there is no fairly simple explanation is that the calculated exchange of potassium ions is higher than that found in *Sepia* axons.

5. It is concluded that the responses of an isolated giant axon of *Loligo* to electrical stimuli are due to reversible alterations in sodium and potassium permeability arising from changes in membrane potential.

REFERENCES

Cole, K. S. (1941). Rectification and inductance in the squid giant axon. *J. gen. Physiol.* **25**, 29–51.

Cole, K. S. & Baker, R. F. (1941). Longitudinal impedance of the squid giant axon. *J. gen. Physiol.* **24**, 771–788.

Cole, K. S. & Curtis, H. J. (1939). Electric impedance of the squid giant axon during activity. *J. gen. Physiol.* **22**, 649–670.

Goldman, D. E. (1943). Potential, impedance, and rectification in membranes. *J. gen. Physiol.* **27**, 37–60.

Hartree, D. R. (1932–3). A practical method for the numerical solution of differential equations. *Mem. Manchr lit. phil. Soc.* **77**, 91–107.

Hodgkin, A. L. (1951). The ionic basis of electrical activity in nerve and muscle. *Biol. Rev.* **26**, 339–409.

Hodgkin, A. L. & Huxley, A. F. (1952*a*). Currents carried by sodium and potassium ions through the membrane of the giant axon of *Loligo*. *J. Physiol.* **116**, 449–472.

Hodgkin, A. L. & Huxley, A. F. (1952*b*). The components of membrane conductance in the giant axon of *Loligo*. *J. Physiol.* **116**, 473–496.

Hodgkin, A. L. & Huxley, A. F. (1952*c*). The dual effect of membrane potential on sodium conductance in the giant axon of *Loligo*. *J. Physiol.* **116**, 497–506.

Hodgkin, A. L., Huxley, A. F. & Katz, B. (1949). Ionic currents underlying activity in the giant axon of the squid. *Arch. Sci. physiol.* **3**, 129–150.

Hodgkin, A. L., Huxley, A. F. & Katz, B. (1952). Measurement of current-voltage relations in the membrane of the giant axon of *Loligo*. *J. Physiol.* **116**, 424–448.

Hodgkin, A. L. & Katz, B. (1949). The effect of temperature on the electrical activity of the giant axon of the squid. *J. Physiol.* **109**, 240–249.

Keynes, R. D. (1951). The ionic movements during nervous activity. *J. Physiol.* **114**, 119–150.

Keynes, R. D. & Lewis, P. R. (1951). The sodium and potassium content of cephalopod nerve fibres. *J. Physiol.* **114**, 151–182.

Lorente de Nó, R. (1947). A study of nerve physiology. *Stud. Rockefeller Inst. med. Res.* **131**, **132**.

Pumphrey, R. J., Schmitt, O. H. & Young, J. Z. (1940). Correlation of local excitability with local physiological response in the giant axon of the squid (*Loligo*). *J. Physiol.* **98**, 47–72.

Downloaded from jp.physoc.org by on January 29, 2008

A quantitative description of membrane current and its application to conduction and excitation in nerve

A. L. Hodgkin and A. F. Huxley

J. Physiol. 1952;117;500-544

This information is current as of January 29, 2008

Updated Information & Services	including high-resolution figures, can be found at: http://jp.physoc.org
Permissions & Licensing	Information about reproducing this article in parts (figures, tables) or in its entirety can be found online at: http://jp.physoc.org/misc/Permissions.shtml
Reprints	Information about ordering reprints can be found online: http://jp.physoc.org/misc/reprints.shtml

Downloaded from jp.physoc.org by on January 29, 2008